Title

EXPERIMENTAL INVESTIGATION OF A POROUS CARBON ELECTRODE FOR THE REMOVAL OF MERCURY FROM CONTAMINATED BRINE

Authors

Matlosz, M.
Newman, J.

Publication Date

1985-07-01

LBL-19611
Preprint

Lawrence Berkeley Laboratory
UNIVERSITY OF CALIFORNIA

Materials & Molecular Research Division

Submitted to Journal of the Electrochemical Society

EXPERIMENTAL INVESTIGATION OF A POROUS CARBON ELECTRODE FOR THE REMOVAL OF MERCURY FROM CONTAMINATED BRINE

M. Matlosz and J. Newman

July 1985

Prepared for the U.S. Department of Energy under Contract DE-AC03-76SF00098

DISCLAIMER

LBL-19611

Experimental Investigation of a Porous Carbon Electrode for the Removal of Mercury from Contaminated Brine

Michael Matlosz[1,*] and John Newman[*]

Materials and Molecular Research Division,
Lawrence Berkeley Laboratory, and
Department of Chemical Engineering,
University of California, Berkeley, California 94720

July, 1985

Abstract

A flow-through porous electrode, made of reticulated vitreous carbon (RVC), has been designed to remove mercury from contaminated brine solutions. Experiments with a bench-scale reactor show that the mercury concentration of contaminated brine solutions can be reduced by as much as a factor of five thousand during a single pass through the electrode. The process is mass-transfer limited, and the results of the experiments are used to develop a general correlation for the dependence of the mass-transfer coefficient on the flowrate of electrolyte through RVC. In addition, the effect of counterelectrode placement on the cell resistance is examined, and the experimental data are compared to predictions from a mathematical model of the system. The model agrees favorably with the experimental results, and the benefits of upstream counterelectrode placement, indicated by the model, are verified.

---

[1]Present address: Ecole Polytechnique Fédérale de Lausanne, Département des matériaux, Laboratoire de métallurgie chimique, 34, chemin de Bellerive, CH-1007, Lausanne SWITZERLAND

[*]Electrochemical Society active member.

Key words: metal recovery, reticulated vitreous carbon, mass-transfer coefficient, flow-through, pollution control.

Introduction

The use of flow-through porous electrodes for the removal of heavy-metal ions from contaminated aqueous solutions has been discussed frequently in the electrochemical literature. The technique has been suggested for the recovery of several heavy-metal pollutants, including copper [1,2], silver [3,4], lead [5,6,7], and antimony [8], as well as mercury [9,10], gold, and cadmium. In all of these systems, the basic principle of separation is the same: the metal is removed by electrodeposition as the solution passes through a porous cathode of high surface area. Since, in many cases, this process allows the heavy metal to be recovered and sold as well as removed from solution, the technique may be economically attractive as an alternative to existing methods of waste removal. Recent reviews of the subject and bibliographic information may be found in [9,11,12,13].

The study described here concerns the removal of mercury from contaminated brine (concentrated saltwater) and follows closely previous investigations of copper removal using a similar technique [1]. The results shown here represent the continuation of an ongoing study of mercury removal, and preliminary results from this laboratory, based on a slightly different reactor design, have been reported previously [10]. This earlier study on mercury indicated that the method is efficient and effective for the decontamination of brine solutions. In addition, the study showed that the mercury deposition system, due to its simplicity, is a good candidate for the general, theoretical study of flow-through porous electrodes. The experimental results of the present work are used to obtain quantitative information regarding the effectiveness of mercury removal under mass-transfer-limited conditions and to verify the applicability of the model of Trainham and Newman [14] to this system.

Electrochemical System

The principal electrochemical reactions that occur in the system are shown below:

Cathode: Mercury Reduction

$$HgCl_4^{-2} + 2e^- \rightarrow Hg(l) + 4Cl^-$$

Anode: Oxygen Evolution

$$2H_2O \rightarrow O_2 + 4H^+ + 4e^-.$$

In all of the experiments presented here, the catholyte was composed of a 4.3 M NaCl solution containing mercury concentrations of between 40 and 55 ppm. Mercury is highly soluble in such chloride solutions due to the complexing of the mercuric ion, and, in the range of concentrations and potentials of this study, $HgCl_4^{-2}$ ion is the predominant mercuric species. The solution was slightly acidic (pH = 4), but hydrogen gas was not generated under typical conditions because the operating potential for the mercury deposition reaction is not sufficiently negative. At the anode, oxygen was evolved from an anolyte of the same salt concentration as the catholyte, but without the mercury. Although chlorine evolution at the anode is possible thermodynamically, none was observed under the conditions of this study.

Figure 1, a plot of the Nernst equation, shows the thermodynamic minimum mercury concentration attainable in a flow-through porous electrode as a function of the potential applied at the catholyte exit. An electrochemical method for the removal of mercury should be effective, since a very low equilibrium mercury concentration exists at a polarization of only a few hundred millivolts. (The abscissa ($V - \Phi_{ref}$) represents the potential of the working electrode with respect to a saturated calomel reference electrode (SCE).) In this study, an inlet concentration of mercury of 40 ppm corresponds to about -5 mV with respect to an SCE.

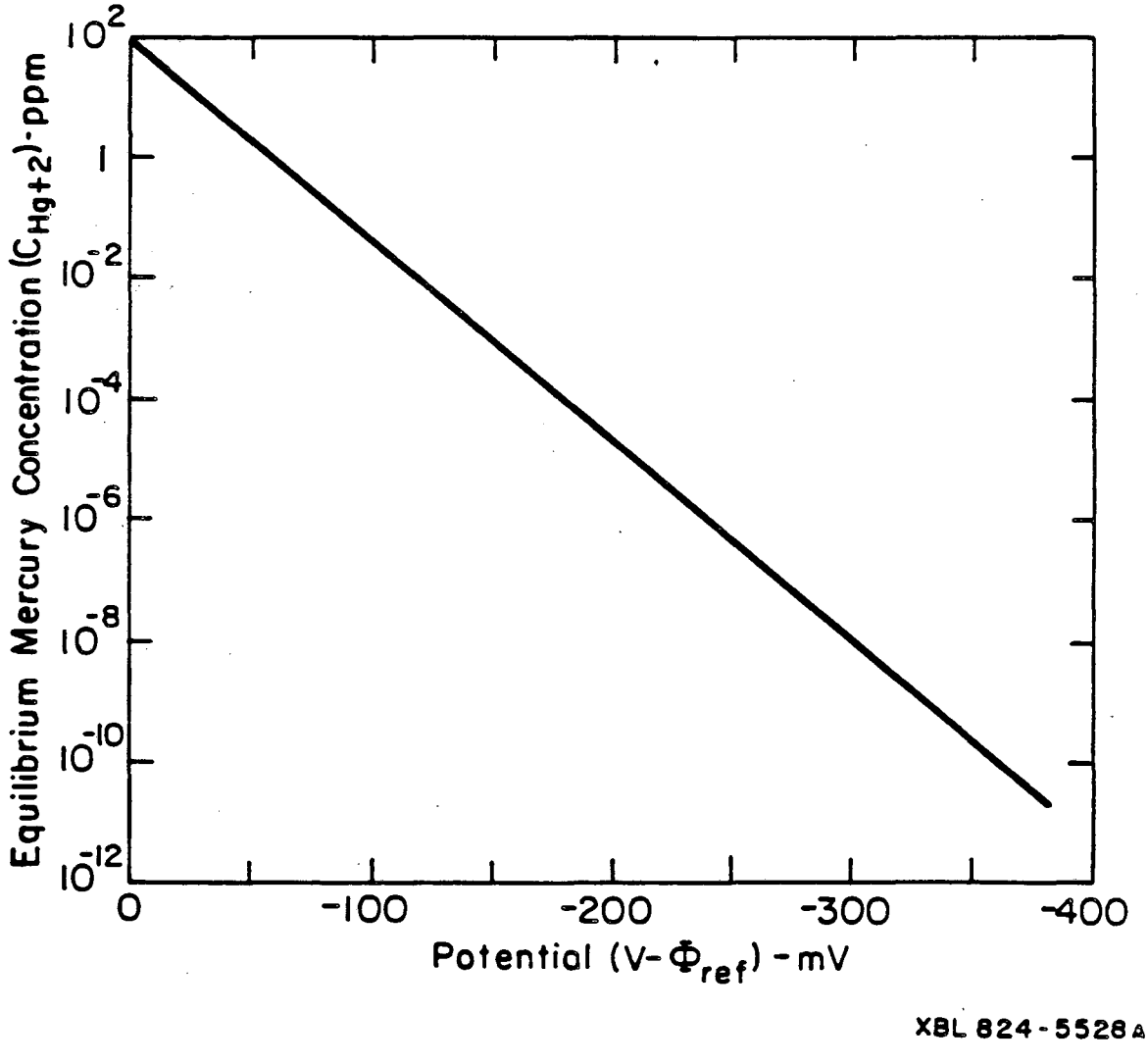

Figure 1. Equilibrium mercury concentration as a function of potential relative to a saturated calomel reference electrode.

Electrode Configuration

Once a decision to attempt an electrochemical method of this type has been made, it becomes necessary to determine the arrangement of the electrodes that will constitute the reactor. Figure 2 shows two possible electrode configurations. Both are considered flow-through, a term indicating that the fluid flow and current flow are parallel. As a result, a one-dimensional model of a flow-through system should provide a suitable theoretical representation of the process. This may be contrasted with so-called flow-by configurations (not shown) in which the fluid flows in a direction perpendicular to the current. Mathematical models of flow-by systems must of necessity be two-dimensional.

Figure 2a shows upstream (before fluid inlet) placement of the counterelectrode, and figure 2b shows downstream placement. If the electrical conductivity of the solid packed bed is much higher than that of the electrolytic solution (which is the case here and is typical of practical porous-electrode systems), much better performance can be expected from upstream placement of the counterelectrode than from downstream placement [11,15]. In the upstream-counterelectrode configuration, lower effluent concentrations are attainable, and the resistance loss (ohmic potential drop) is smaller than in the case of downstream placement. This smaller ohmic potential drop allows reactors with upstream placement to be operated at much higher flowrates without side reactions. Therefore, because of its practical importance, upstream-counterelectrode placement is emphasized in this study, and experiments involving downstream placement are presented only to demonstrate the effect of electrode placement on the ohmic potential drop.

Experimental Porous Electrode

Figure 3 shows a sketch of the experimental reactor. The cathode compartment is a plexiglass tube, two inches in diameter. A five-inch-long cylinder of

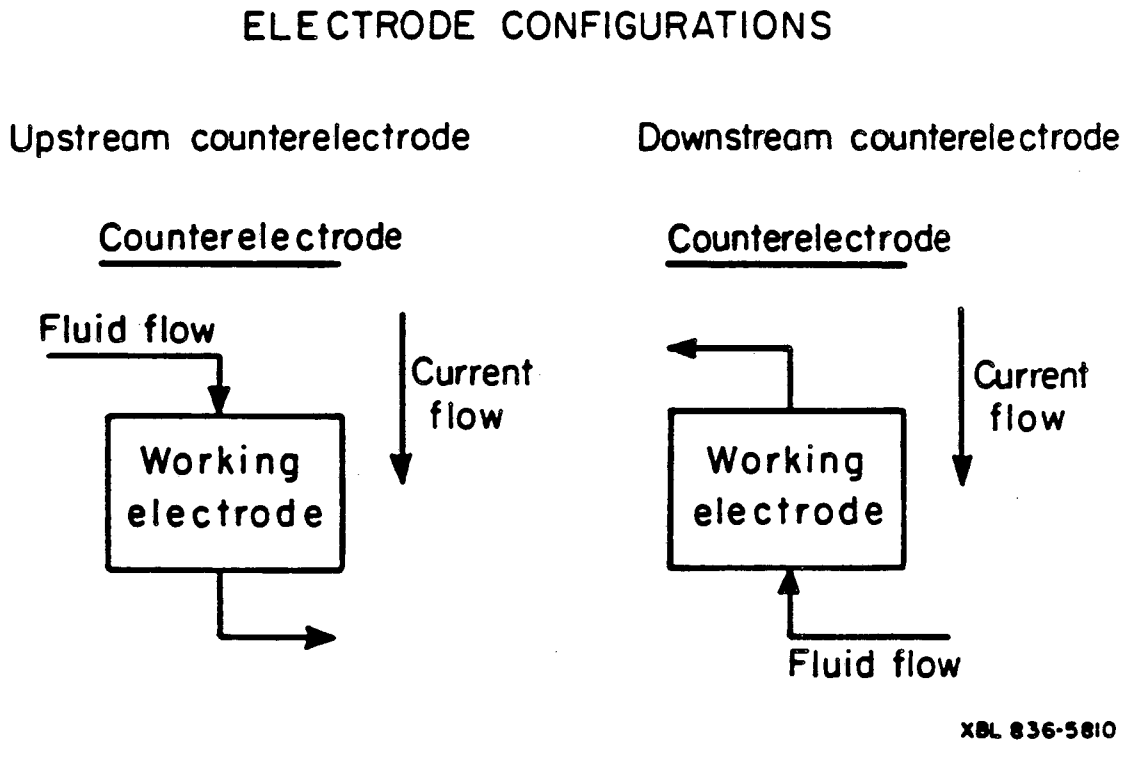

Figure 2. Counterelectrode configurations in a flow-through porous electrode system. (2a) Upstream counterelectrode placement. (2b) Downstream counterelectrode placement.

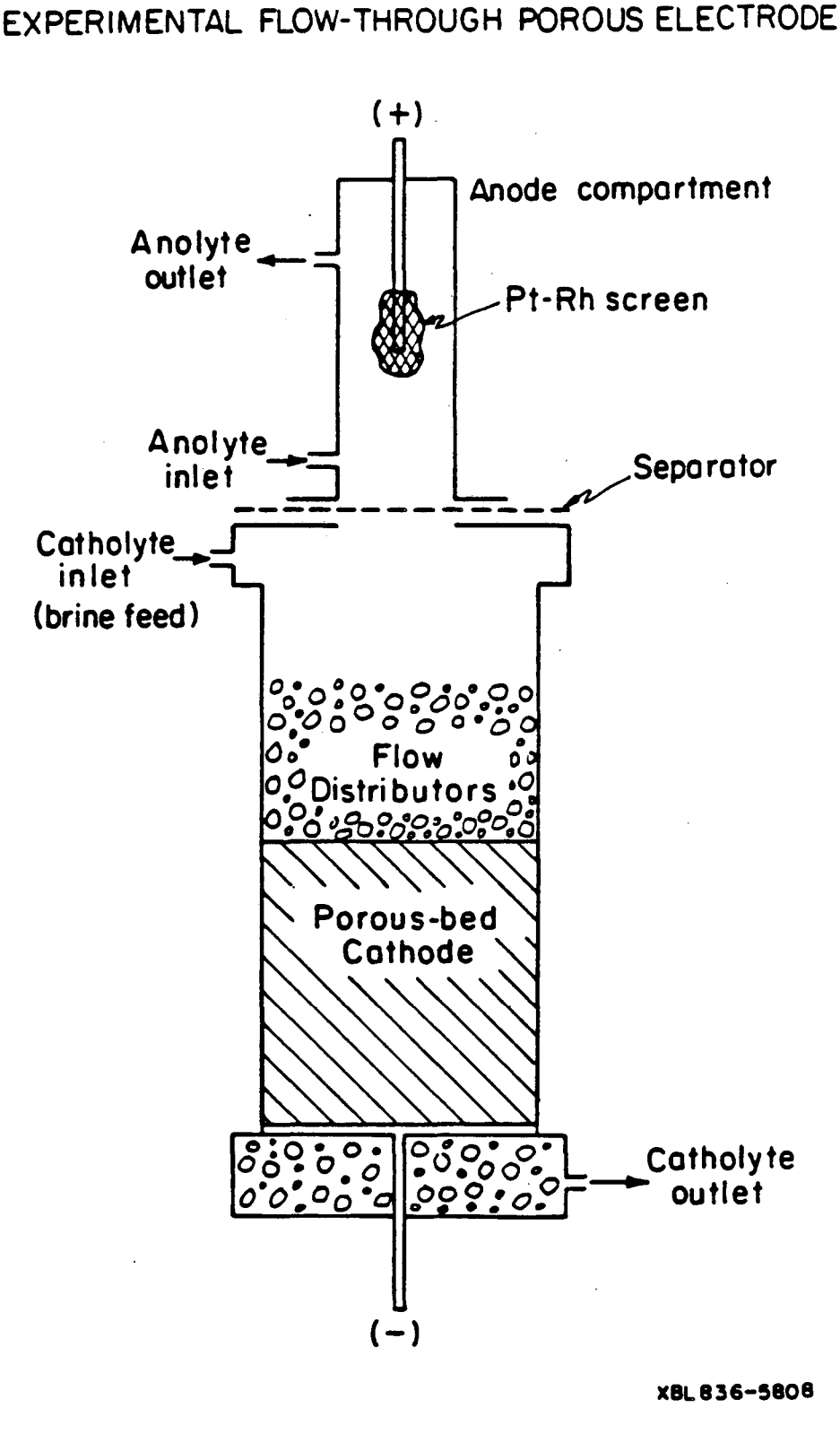

Figure 3. Sketch of the experimental flow-through porous electrode reactor.

RVC (E. R. G., Inc., Oakland, California) forms the working electrode (cathode), which is fitted atop a perforated current-collector plate. The anode compartment, a one-inch-diameter plexiglass tube, is separated from the cathode compartment by a Nafion® membrane separator, and the counterelectrode (anode) is a Pt/Rh screen, spot-welded to a current-collector rod.

Isolation of the two electrode compartments permits independent control of the flows of anolyte and catholyte by two metering pumps (Fluid Metering, Inc.). Oscillations in the catholyte flowrate are removed by a flow damper placed after the catholyte pump, and the catholyte flowrate is measured by a rotameter (Gilmont Instruments, Inc.). Glass beads, placed above and below the carbon bed, distribute the fluid flow.

The anode and cathode current collectors are both made of tantalum (rather than stainless steel) to avoid corrosion due to the high chloride-ion concentration in solution. The flow system is constructed of Bev-A-Line® chemical-resistant tubing connected by polypropylene tubing connectors. During the experiments, the feed solutions are sparged with nitrogen to remove oxygen that might be reduced at the cathode.

Two reference electrodes (Corning Saturated Calomel Reference Electrodes) are placed in the system to monitor the solution potential. An upstream reference potential is measured from a capillary placed in the cell above the carbon bed, and a downstream reference potential is measured at the catholyte outlet. All experimental polarization curves are obtained under potentiostatic control, where the potential of the working electrode (cathode) with respect to the saturated calomel reference electrode in the exit stream is regulated by an AIS Model V-2LR-D Potentiostat.

Photographs of the reactor, the carbon electrode, and the flow system are shown in [6], which describes additional experiments, with the same reactor, for lead removal from contaminated sulfuric acid solutions.

Electrode Operation and Concentration Measurement

Figure 4 illustrates the general operation of the porous electrode. To remove mercury, the working electrode is polarized cathodically, and current is drawn from the current collector. Mercury is deposited onto the surface of the electrode as the contaminated solution passes through it, and oxygen is evolved at the counterelectrode. Once a solution has been purified, the mercury can be recovered, and the electrode can be regenerated, by reversing the polarization of the cell. Thus, in the regeneration operation, the working electrode is polarized anodically, mercury on the electrode surface is dissolved, and hydrogen is evolved on the counterelectrode.

Since the mercury can be stripped very quickly and easily from the electrode during the regeneration step, this process provides a convenient method for concentrating dilute mercuric chloride solutions. Initially, the dilute solution can be purified (and the mercury stored on the electrode surface). Then, by decreasing the flowrate of brine through the electrode during the regeneration step, a small volume of concentrated mercuric chloride solution can be obtained, from which product mercury may be recovered by conventional electrowinning techniques.

This two-step procedure has many practical applications, and, although this study focuses principally on the mercury-deposition (purification) step, bed regeneration was in fact used in the laboratory. By recovering the metal as described above, mercury deposited onto the RVC in one experiment could be reused in another, the pore characteristics of the RVC were preserved, and pore plugging was avoided.

Accurate analysis of the concentration of mercury in the effluent solutions was essential if the experimental results were to be useful for process scale-up. Unfortunately, because of the extremely low concentrations of mercury (low ppb) as well as the high concentration of chloride ion (4.3 M), conventional

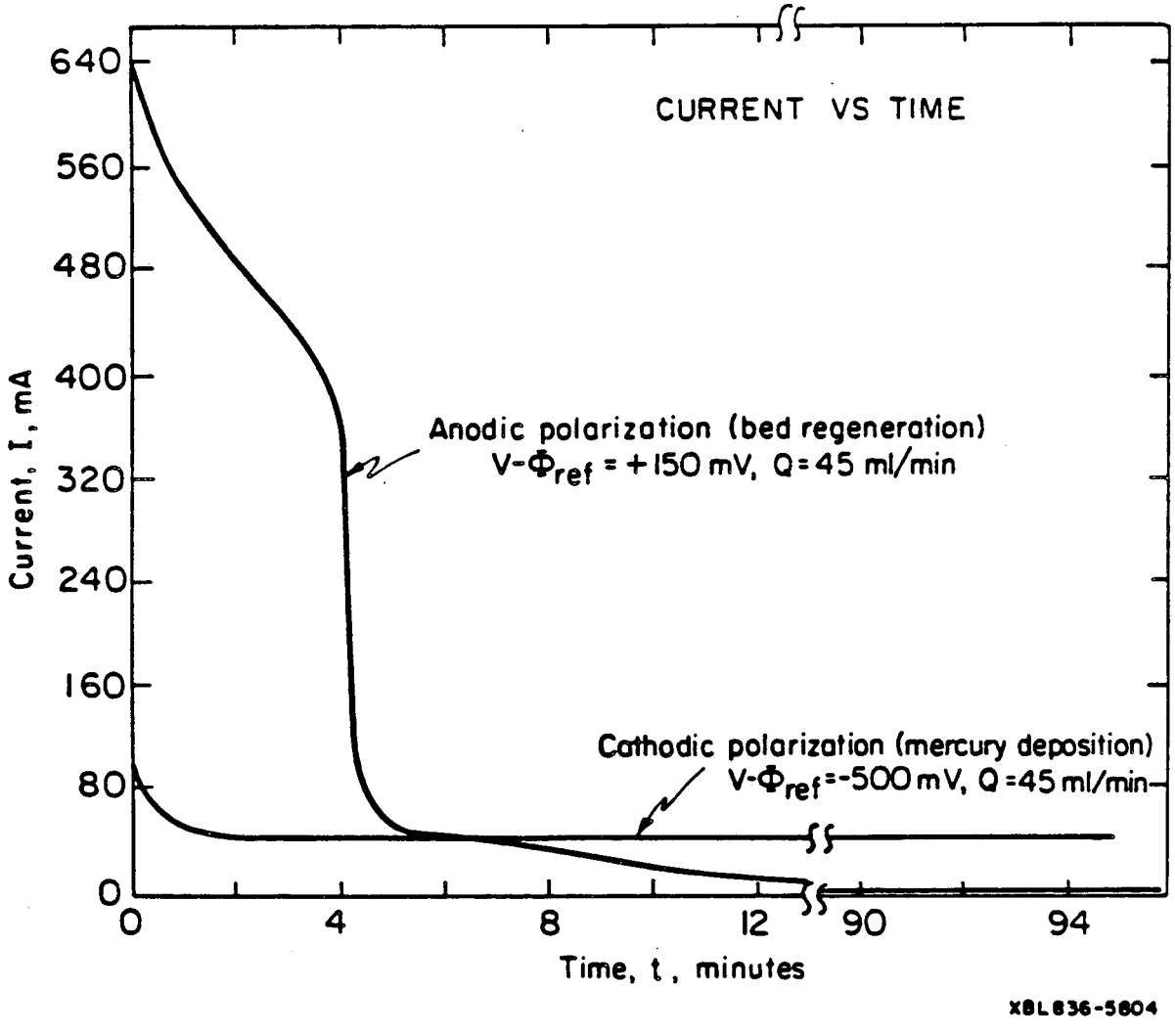

Figure 4. Current to the porous electrode as a function of time. (Current is plotted as the absolute value.)

measurement techniques (such as atomic absorption spectrophotometry) were not adequate. As a result, it was necessary to employ a more sensitive method for the measurements -- a gold-film mercury analyzer.

The gold-film analyzer measures the change in the electronic resistance of a piece of gold foil upon contact with an air stream containing mercury vapor, and the instrument is sensitive to as little as one nanogram of elemental mercury. In addition, since the resistance change is due to the amalgamation of the mercury with the gold (a process unique to mercury), the measurement is specific and free of interferences.

For this study, mercury concentrations in all of the liquid samples were measured with a Jerome Instruments, Inc., Model 301 Gold Film Mercury Analyzer according to the procedure outlined in [16]. First, mercuric ions in the liquid samples were chemically reduced (with $SnCl_2$) to elemental mercury. Next, the reduced solution was sparged with a pure air stream in order to liberate mercury vapor, and the air stream was then passed to the analyzer, where the total mass of mercury was measured. Finally, the mercury concentration was determined from the mass of mercury vapor detected divided by the volume of the original (liquid) sample. With this technique, mercury concentrations from one part per thousand down to five hundred parts per trillion could be measured to an accuracy of about ten percent.

Experimental Results From the RVC Reactor

Steady-State Polarization Behavior

Figures 5 and 6 show the steady-state polarization behavior for mercury deposition in the RVC reactor for both the upstream- and downstream-counterelectrode configurations. The points are the polarization measurements, and the numbers below the points show the experimentally determined mercury

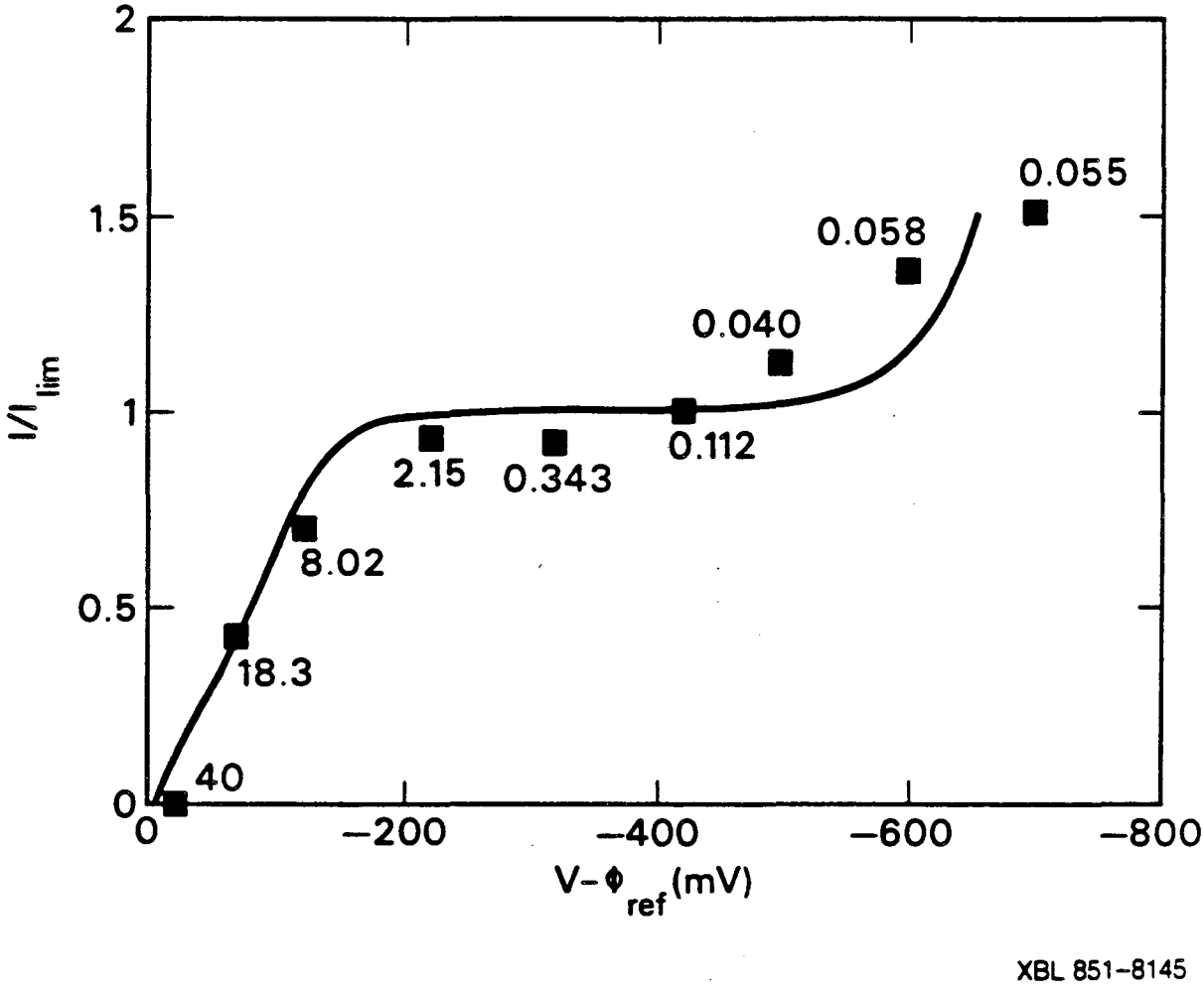

Figure 5. Polarization curve for the reactor with upstream counterelectrode placement. Q = 30 cm^3/min, L = 12.7 cm, Feed concentration = 40 ppm Hg (c_{Rf} = 2.273 ×10^{-7} mol/cm^3). The points are experimental measurements, and the curve represents the model. Numbers below the points show experimentally measured effluent concentrations.

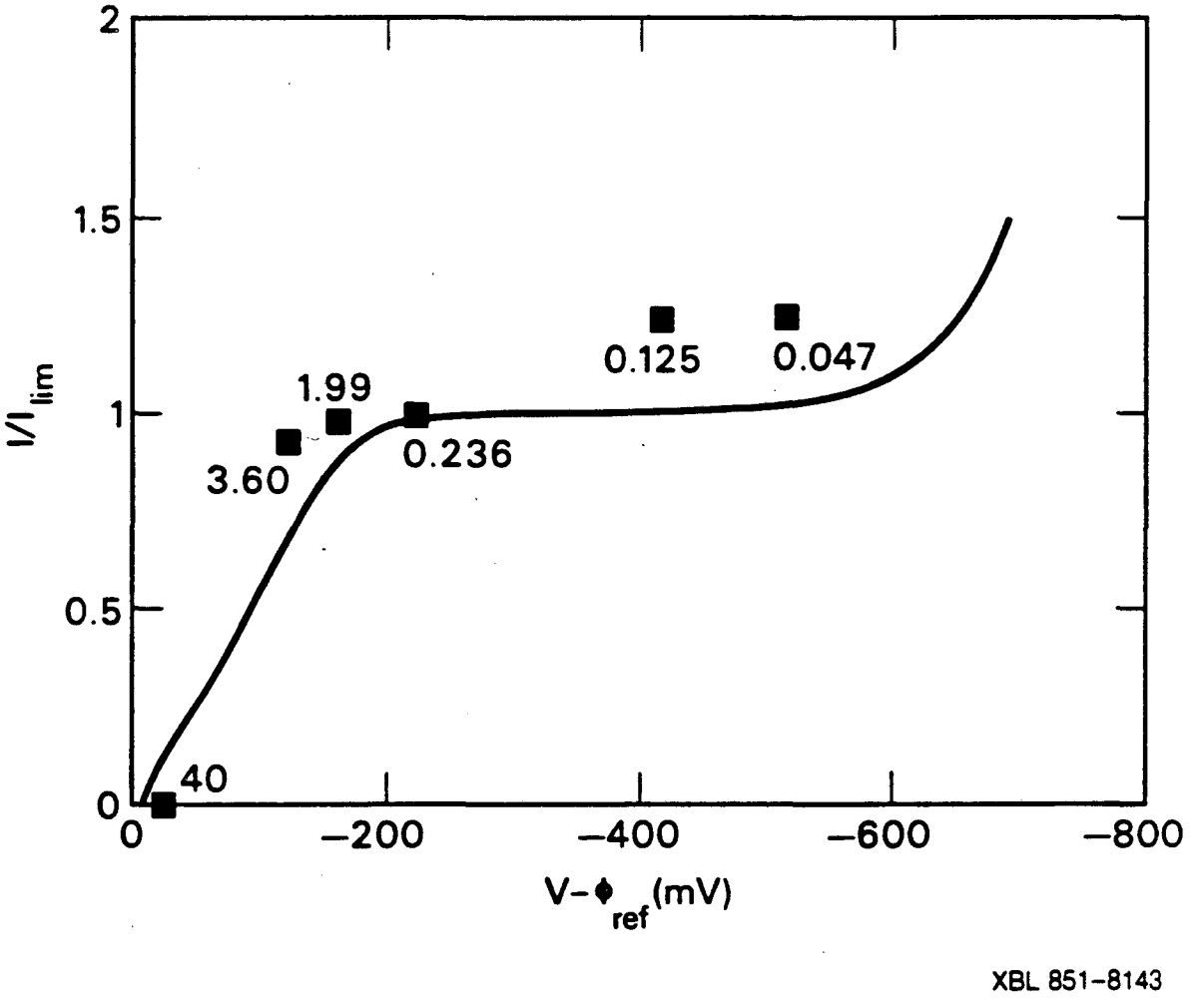

Figure 6. Polarization curve for the reactor with downstream counterelectrode placement. Q = 30 cm^3/min, L = 12.7 cm, Feed concentration = 40 ppm Hg (c_{Hg} = 2.273 $\times 10^{-7} mol/cm^3$). The points are experimental measurements, and the curve represents the model. Numbers below the points show experimentally measured effluent concentrations.

concentration (in ppm) at the catholyte exit. The curves on the figures represent predictions from the mathematical model.† Flat limiting-current plateaus were obtained with only moderate polarization, indicating that the major limitation to mercury removal is the rate of mass transfer of the mercuric-ion complex to the surface of the cathode pore. In a typical experiment, about 3000 to 5000 cm^3 of solution were passed before steady state was achieved. Thus, in this case, for a flowrate of 30 cm^3/min, each point on the polarization curve required 100 minutes of stable operation of the reactor. Sparging of the catholyte feed with nitrogen reduced the oxygen content of the incoming brine, and faradaic current efficiencies of about 90 percent were achieved routinely. At high polarization (above -500 mV), the increase in current is due to the production of dissolved hydrogen gas. Hydrogen bubbles, however, were not produced, since the amount of gas generated was well below the solubility limit. Table 1 indicates pertinent physical property data†† and operating conditions for the measurements shown in figures 5 and 6.

Table 1. Physical Property Data and Operating Conditions

a =	66 cm^2/cm^3	U_R^0 =	0.4138 V ($HgCl_4^{-2}/Cl^-/Hg$)
D_o =	1.0×10^{-5} cm^2/s	U_S^0 =	0.000 V (H^+/H_2)
ϵ =	0.97	U_{re} =	0.2415 V (Calomel, Sat'd KCl)
ρ_o =	1.14×10^{-3} kg/cm^3	μ =	1.52×10^{-2} g/cm–s
ν =	1.333×10^{-2} cm^2/s	κ_o =	0.199 mho/cm
σ =	1.73 mho/cm	Sc =	1333
c_{Rf} =	2.273×10^{-7} mol/cm^3	c_{a-f} =	4.3×10^{-3} mol/cm^3
L =	12.7 cm	pH =	4.0
P_{H_2f} =	5×10^{-7} atm	S =	20.26 cm^2
T =	298.15 K	v =	0.0255 cm/s
$\bar{k}_m$ =	2.102×10^{-4} cm/s	Re =	0.02811
Pe =	38.64	Sh =	0.3089

† A discussion of the fitting parameters used for the model predictions is presented later.

†† Values of U_S^0, U_{re}, ρ_o, μ, ν, κ_o, and P_{H_2f} are taken from [17]; a, ϵ, and σ from [18]; U_R^0 from [9]. Other values were measured in the laboratory.

Effect of Counterelectrode Placement

Figure 7 demonstrates the effect of counterelectrode placement on the resistance to current flow within the porous electrode. The abscissa is the applied potential (in mV) between the working (porous) electrode and a saturated calomel reference electrode at the catholyte exit. The ordinate represents the effective area-specific resistance,

$$\frac{\Phi_{upstream} - \Phi_{downstream}}{i},$$

and has units of ohm-cm^2. As in figures 5 and 6, the points are the experimental measurements, and the curves represent model predictions. (During the experiments, the tip of the capillary from the upstream reference electrode was located a distance of 1 cm above the porous electrode, within the flow distributors, resulting in an uncompensated resistance of 30 ohm-cm^2.† This value is added to the resistance calculated from the model.)

Although the removal effectiveness is approximately the same for both cases (see figures 5 and 6), it can be seen that downstream placement causes a considerable increase in ohmic potential drop. This difference can be understood by considering the concentration distribution through the electrode under mass-transfer-limited conditions. In the absence of axial diffusion and dispersion effects, the concentration drops exponentially with length x through the electrode, as represented by the following relation [1]:

$$\frac{c_R(x)}{c_{Rf}} = \exp\left(-\frac{ak_m x}{v}\right), \qquad (1)$$

where k_m represents a local mass-transfer coefficient, assumed to be constant throughout the length of the reactor. Examination of this relationship reveals that the majority of the mercuric-ion complex has been removed within a short

† The glass beads represent a bed of uniformly packed spheres, $\epsilon = 0.3$. (The effective conductivity, κ, is calculated as shown in table 3.)

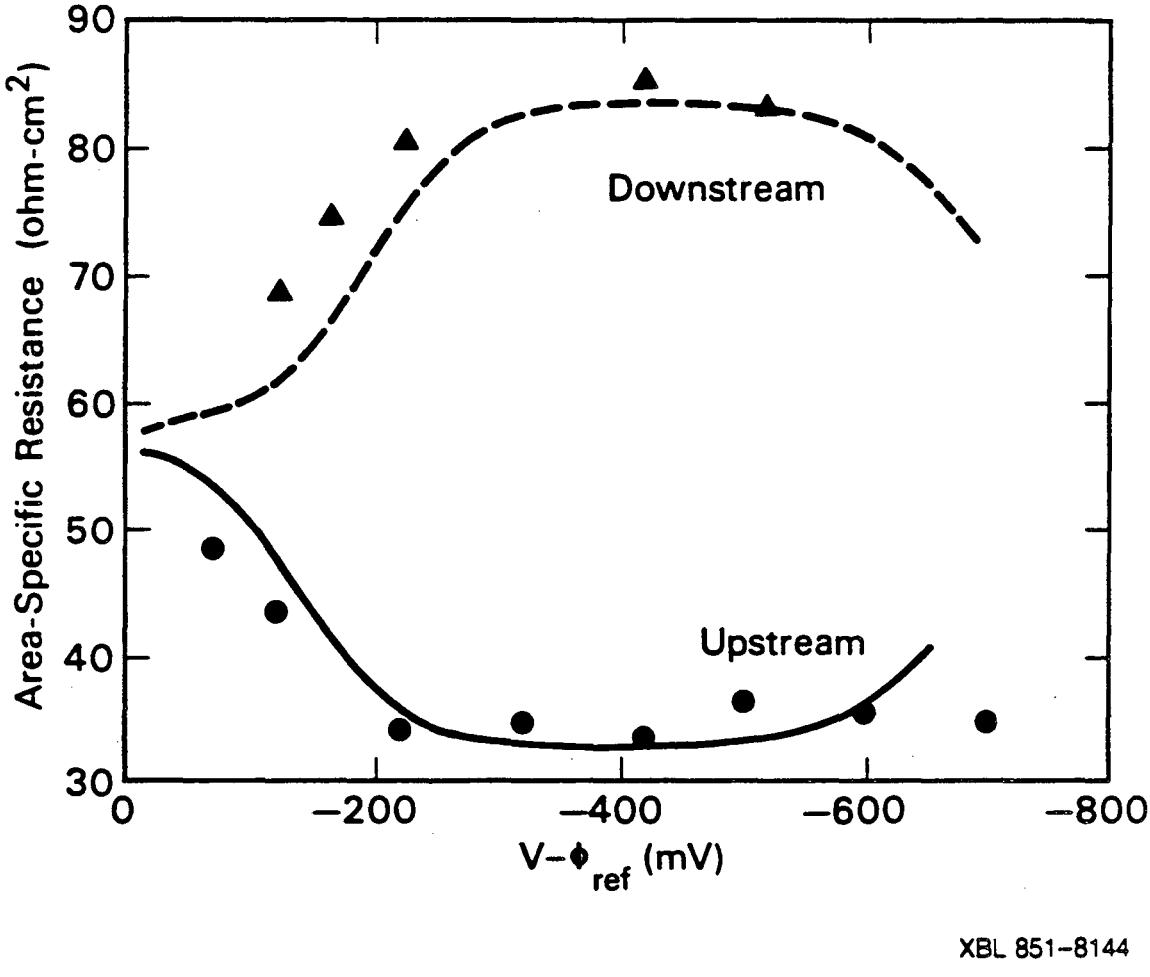

Figure 7. Effect of counterelectrode placement on the area-specific solution resistance within the porous electrode. (Operating conditions are identical to those in figures 5 and 6.) The points are experimental measurements, and the curves represent the model.

distance, of order v/ak_m, of the entrance to the reactor. Thus, the bulk of the charge transfer occurs in a region generally much shorter than the total length of the reactor, L. Although the additional length is necessary when high removal effectiveness is desired, the reduction of trace amounts of mercury further along the reactor contributes only a small fraction to the total charge transfer.

Figure 8 illustrates the effect of counterelectrode placement on the overall resistance by showing the "effective" current path through the electrolyte for the two cases. In the case of upstream placement, the current must travel only a distance equivalent to approximately v/ak_m, whereas in the case of downstream placement, the current path is approximately equivalent to the length of the reactor, L. If high removal effectiveness is desired, then L will be much greater than v/ak_m, and, consequently, the resistance will be much higher for downstream placement than for upstream placement of the counterelectrode. (Only the current path through the electrolyte is considered here, since the conductivity of the carbon bed is much higher than that of the electrolyte. If the conductivity of the electrode matrix is of the same order as that of the electrolyte, then the placement of the cathode current collector is also important. For a discussion of this effect, see [15].)

In general, the additional cell resistance in the case of downstream placement causes difficulties in the operation of the reactor, since the possibility of a side reaction is increased considerably. Furthermore, this increased likelihood of side reaction has a direct effect upon the reactor design. In particular, for high removal efficiency, the current density is directly proportional to the flowrate of catholyte, and the ohmic potential drop is directly proportional to the current density. Thus, if the ohmic potential drop, $\Phi_{upstream} - \Phi_{downstream}$, must be kept below some critical value in order to avoid side reactions, the maximum permissible flowrate is higher with upstream counterelectrode placement than with downstream placement. In short, the higher resistance in the downstream

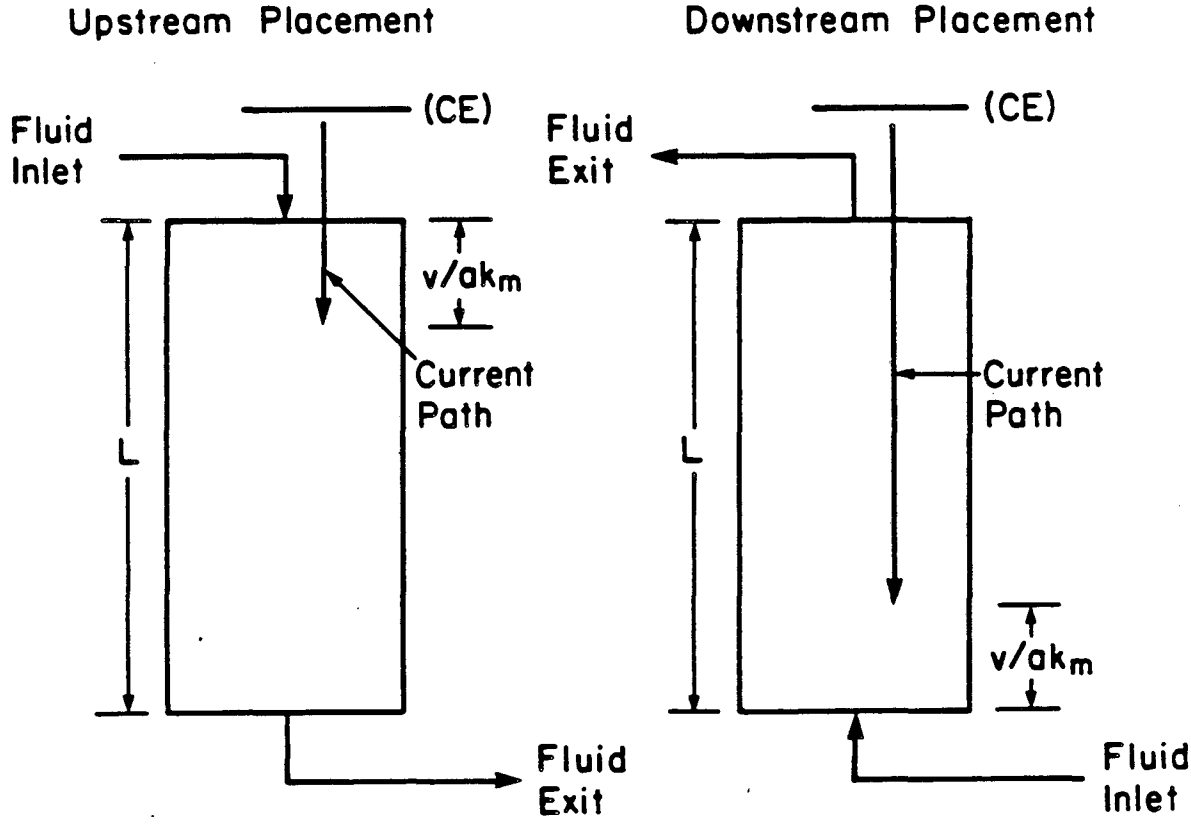

Figure 8. Sketch of the effect of counterelectrode placement on the effective current path through the electrolyte.

counterelectrode configuration limits the throughput of the reactor [1,11].

Under the conditions of this study, mercury removal is not affected by counterelectrode placement (see figures 5 and 6), since a very high overpotential is required for the production of hydrogen and the flowrates are not near their limiting values. Nevertheless, the resistance measurements shown in figure 7 indicate that, in this reactor, the maximum permissible flowrate for the upstream-counterelectrode configuration is significantly larger than that for the downstream configuration. The remainder of the results presented in this paper will be restricted to cases of upstream counterelectrode placement in the reactor.

Effect of Catholyte Flowrate

Figure 9 illustrates the effect of catholyte flowrate on the limiting current. As before, both the experimental data and the model predictions are shown. Since the removal of mercury is very nearly complete, the limiting current increases proportionately with catholyte flowrate.

The effect of catholyte flowrate on the effluent concentration (at limiting current[†]) is summarized in figure 10 and table 2 for seven experimental runs. Increased convection in the cathode pores at higher flowrates reduces the mass-transfer resistance. Nevertheless, the effect of the associated decrease in residence time is greater, and, therefore, the effluent contains more mercury at the higher flowrates.

The effectiveness of this method of removing mercury from contaminated solutions is clearly demonstrated by these results. At the lowest flowrate examined (10 cm^3/min), a decrease of a factor of 5000 in the mercury concentration was achieved, indicating that this method is a feasible alternative to existing chemical methods of mercury removal.

[†] All limiting-current data were obtained at a polarization, ($V-\Phi_{ref}$), of -500 mV.

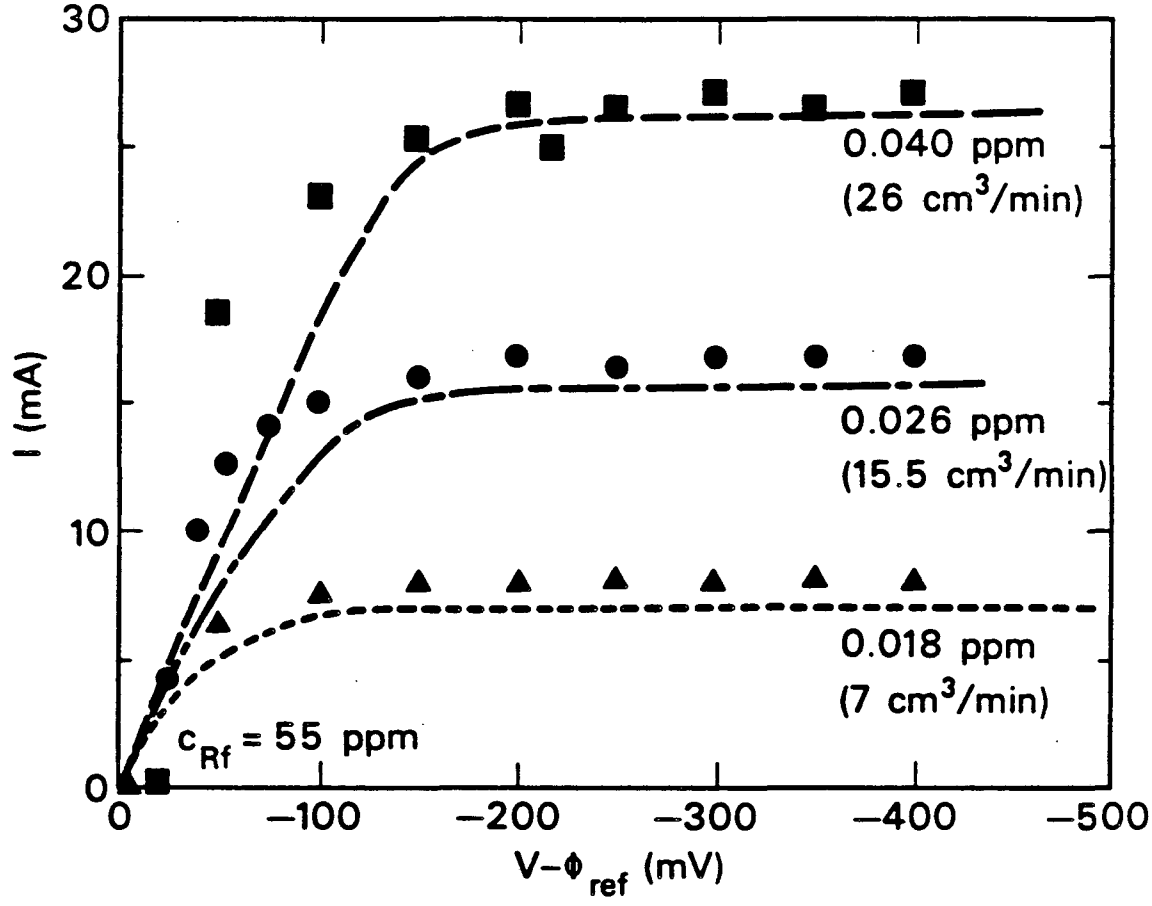

Figure 9. Polarization curves as a function of catholyte flowrate. L = 12.7 cm, feed concentration = 55 ppm Hg. The points are experimental measurements, and the curves represent the model.

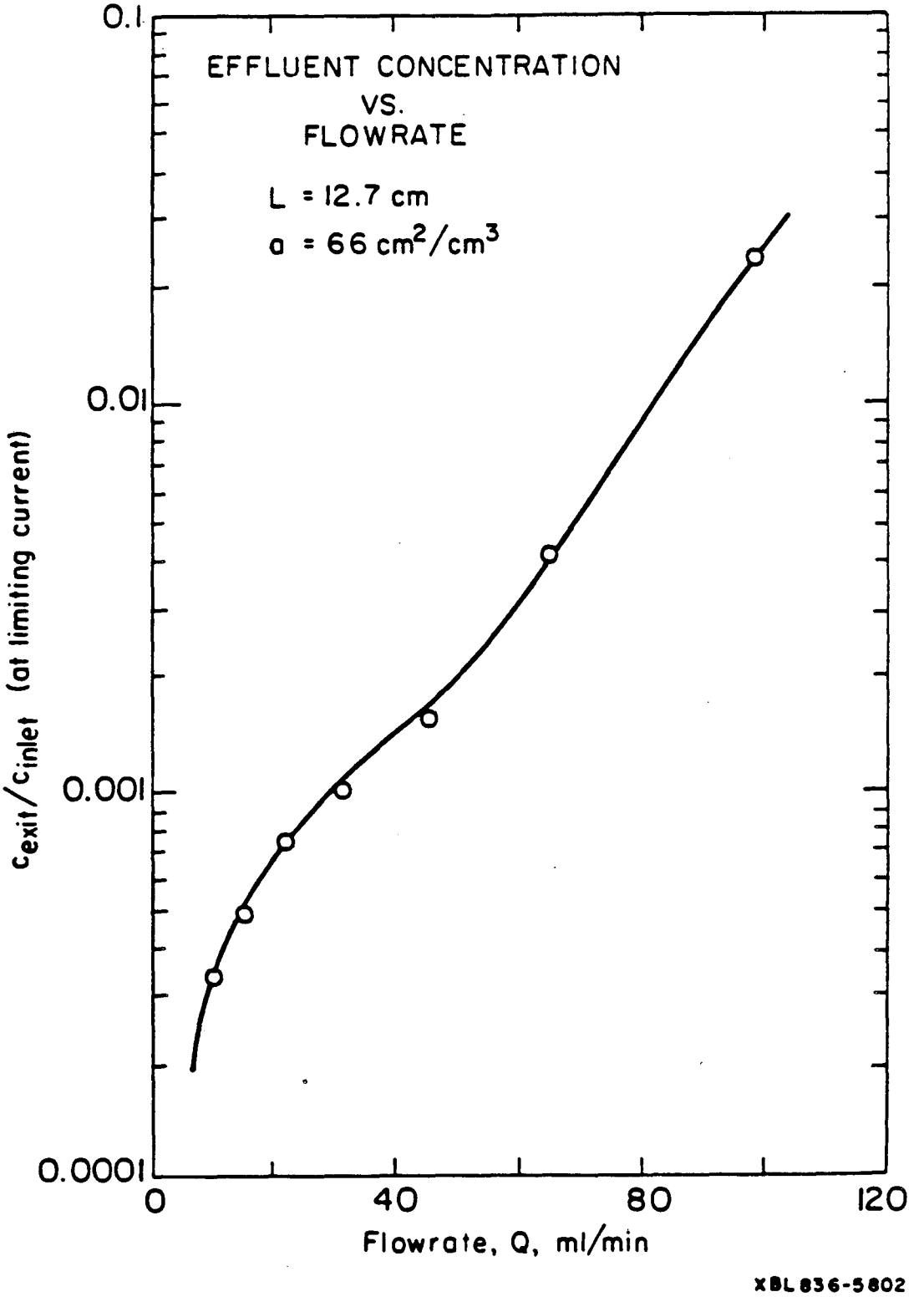

Figure 10. Effect of flowrate on the effluent concentration at limiting current.

Table 2. Effect of Flowrate on Effluent Concentration at Limiting Current

Q (cm^3/min)	v (cm/s)	c_{Rf} (ppm Hg)	$c_R(L)$ (ppm Hg)	$\bar{k}_m$ (cm/s)
98	0.0806	26	0.606	3.615×10^{-4}
65	0.0534	65	0.262	3.513×10^{-4}
45	0.0370	110	0.168	2.862×10^{-4}
31	0.0255	59	0.0588	2.102×10^{-4}
22	0.0181	42	0.0303	1.562×10^{-4}
15	0.0123	56	0.0262	1.125×10^{-4}
10	0.00822	55	0.0180	7.870×10^{-5}

Definition of the Mean Mass-Transfer Coefficient

Equation (1) can be used to develop the following general definition:

$$\bar{k}_m = -\frac{v}{aL}\ln\left(\frac{c_R(L)}{c_{Rf}}\right), \tag{2}$$

where the mean mass-transfer coefficient, $\bar{k}_m$ (unlike the local coefficient, k_m) may contain the effects of axial diffusion and dispersion. $\bar{k}_m$ is more convenient than k_m for tabulation, since its use does not require an independent value of the dispersion coefficient [11,19]. The mean mass-transfer coefficient, $\bar{k}_m$, in general, depends on the diffusion coefficient (D_o), the solution velocity (v), the viscosity (μ), and the electrode geometry (pore structure). Therefore, a generalized dimensionless correlation of the effect of velocity on the mass-transfer coefficient in RVC can be developed from the results of these experiments, provided that independent measurements of the surface area per unit volume of reactor (a) and the diffusion coefficient (D_o) are available. Reticulated vitreous carbon has a uniform pore structure, and the value of surface area per unit volume is available [18]. The value of the diffusion coefficient, however, has not

been measured, and it was therefore decided to determine its value in an independent experiment.

Measurement of the Diffusion Coefficient

The diffusion coefficient of the mercuric chloride complex was obtained from the limiting current to a rotating disk electrode. For a single-electrode reaction on the surface of a disk, an integral-average diffusion coefficient of the electro-active species in solution can be determined from the Levich relation shown below [20]:

$$I_{\text{lim}} = 0.620 n F A D_o^{2/3} \Omega^{1/2} \nu^{1/6} c_b . \qquad (3)$$

A plot of the mass-transfer-limited current, I_{lim}, versus the square root of the angular velocity, $\Omega^{1/2}$, is a straight line, and the diffusion coefficient may be obtained directly from the slope.

Figure 11 shows a sketch of the apparatus used for the rotating-disk experiments. A Pine Instruments potentiostat regulated the potential of the working, glassy-carbon electrode (A = 0.442 cm^2) with respect to a saturated calomel reference electrode in the side arm. Figure 12 shows the resulting polarization curves (for a sweep rate of 5 mV/sec). Flat, stable limiting-current plateaus were obtained, and a plot of the limiting current as a function of the square root of rotation speed† is shown in figure 13 for a concentration of 150 ppm Hg in 3.8 M NaCl. From the slope of the plot, a diffusion coefficient of $(1.0 \pm 0.2) \times 10^{-5}$ cm^2/s was determined.

† Notice that, in figure 13, Ω is expressed in revolutions per minute (rpm).

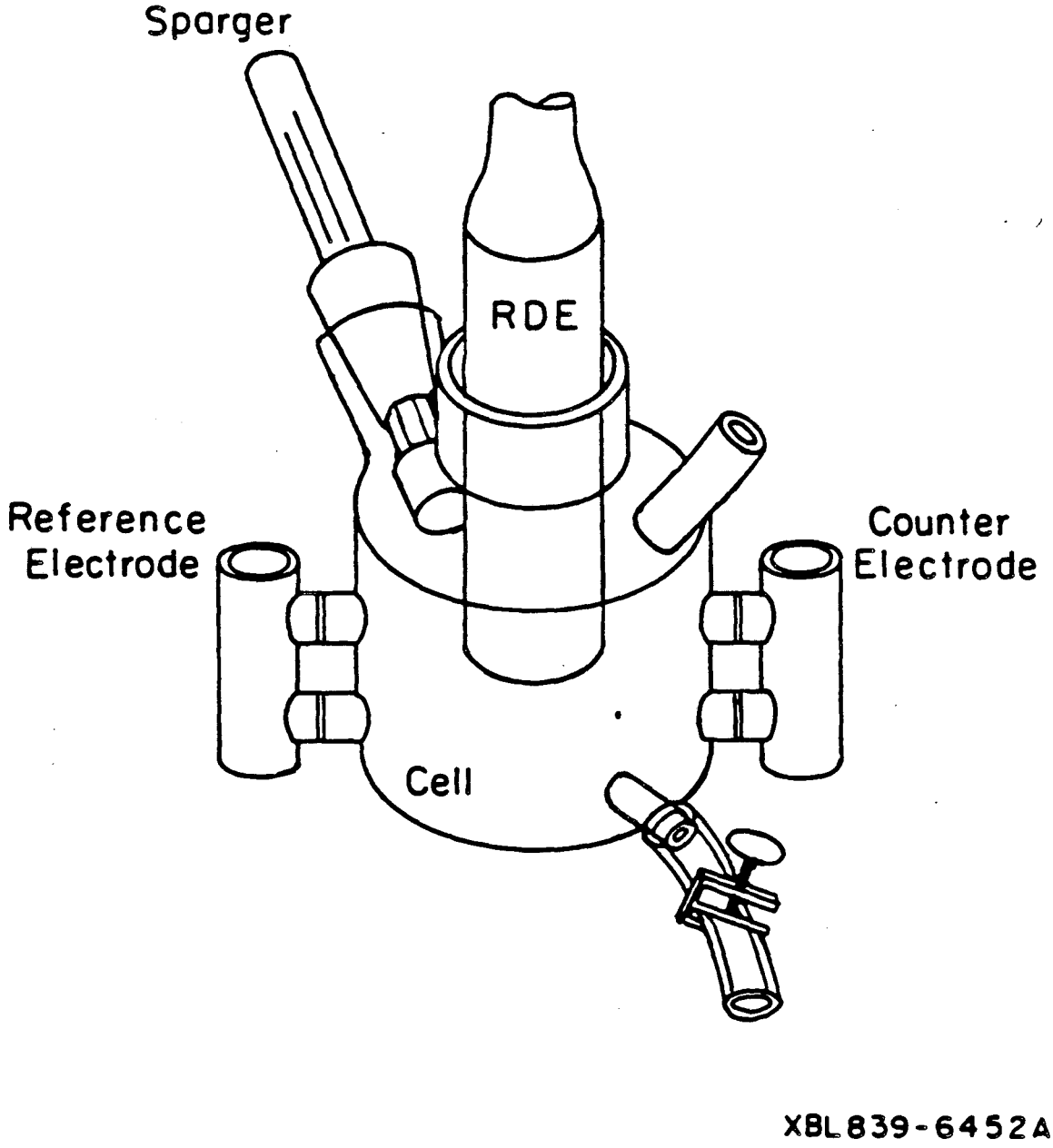

Figure 11. Sketch of rotating disk electrode apparatus.

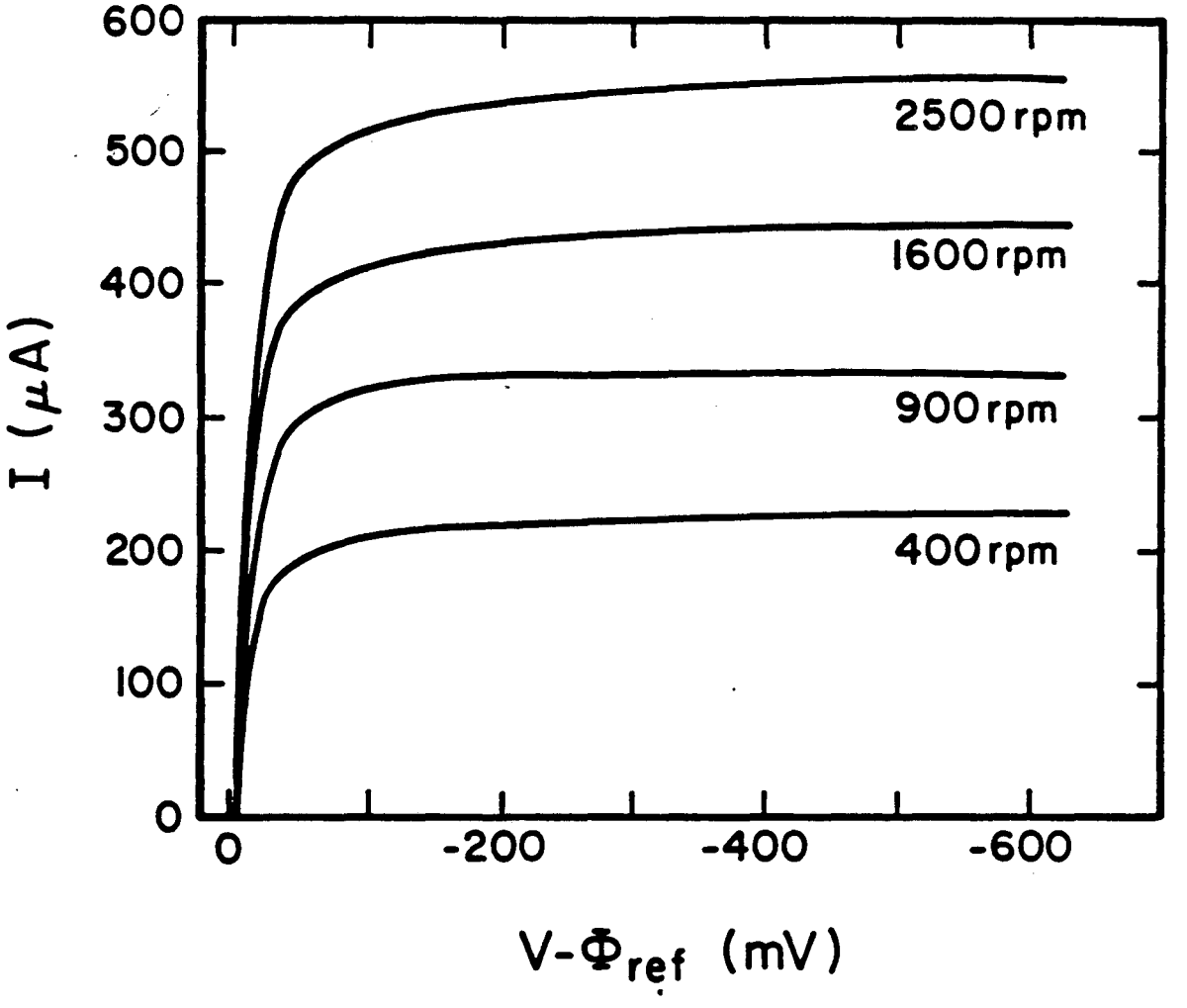

Figure 12. Polarization curves as a function of rotation speed. c_b = 5×10^{-7} mol/cm^3, $c_{Cl^-} = 3.8\times10^{-3}$ mol/cm^3.

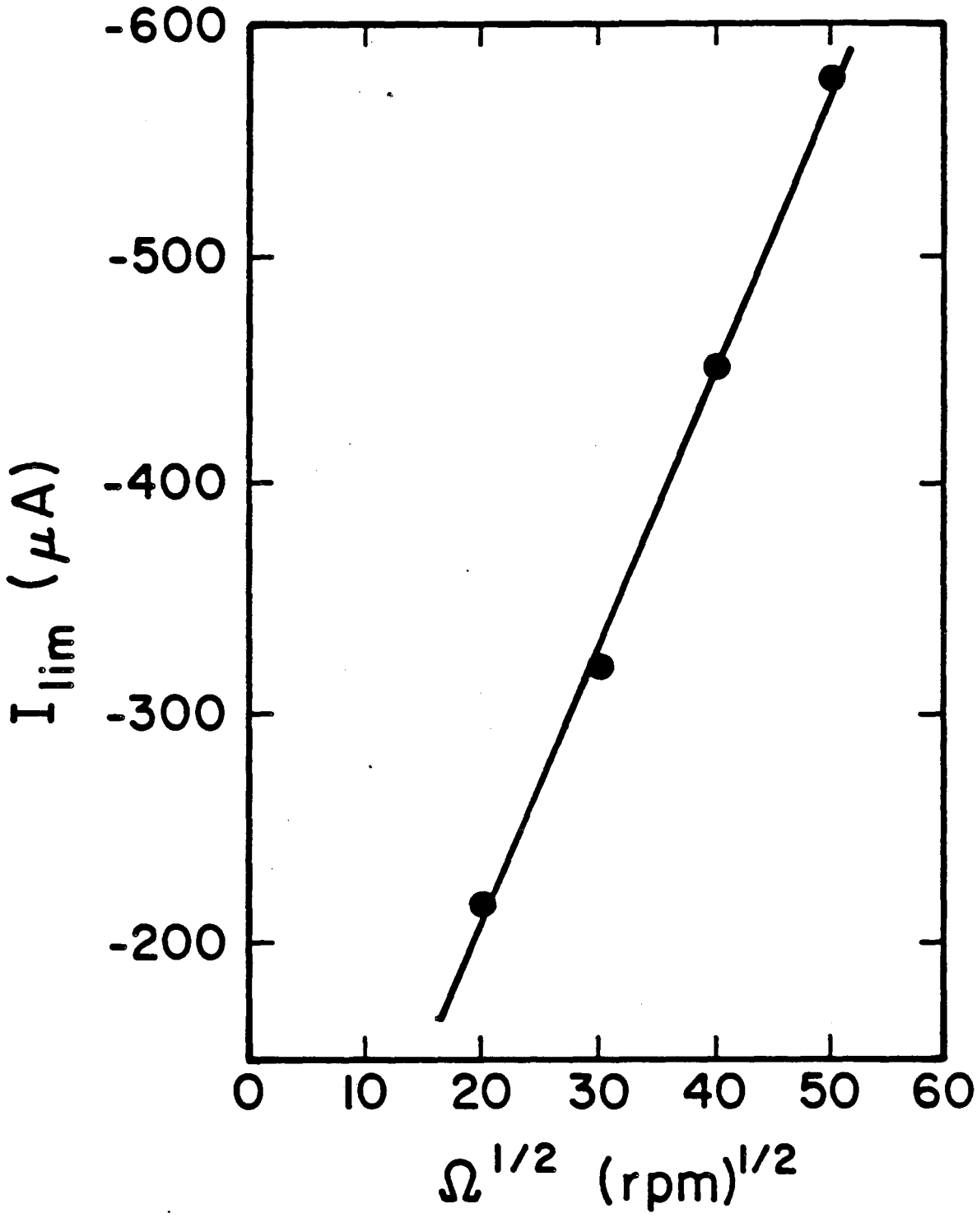

Figure 13. Limiting current versus square root of rotation speed.

Generalized Correlation for the Mass-Transfer Coefficient

If the velocity and mass-transfer coefficient are non-dimensionalized with respect to a characteristic length (a^{-1}) and diffusion coefficient (D_o), then a correlation of the behavior of the mass-transfer coefficient as a function of velocity should depend only on geometric factors (*i. e.*, pore structure of the RVC). Such a plot can now be obtained from the experimental results of the porous-electrode experiments, and it is shown in figure 14. The dimensionless mass-transfer coefficient, or Sherwood number (Sh), defined as

$$Sh = \frac{\epsilon \bar{k}_m}{aD_o}, \tag{4}$$

is shown on the ordinate, and the dimensionless velocity, or Péclet number (Pe), defined as

$$Pe = Re \cdot Sc = \frac{v}{aD_o}, \tag{5}$$

is shown on the abscissa.

At low values of the Péclet number, the logarithm of the Sherwood number varies linearly with the logarithm of the Péclet number (with a slope of approximately one), and, as the Péclet number is increased, the Sherwood number gradually becomes independent of Péclet number. This behavior is characteristic of mass-transfer coefficients in packed beds, and it indicates a transition from a region where axial dispersion effects are important (low Péclet number) to a region where such effects can be neglected [21].

Since this correlation is general and depends only on the geometry of the RVC, it may be used in the scale-up and design of other reactors fabricated from RVC for metal-removal applications.

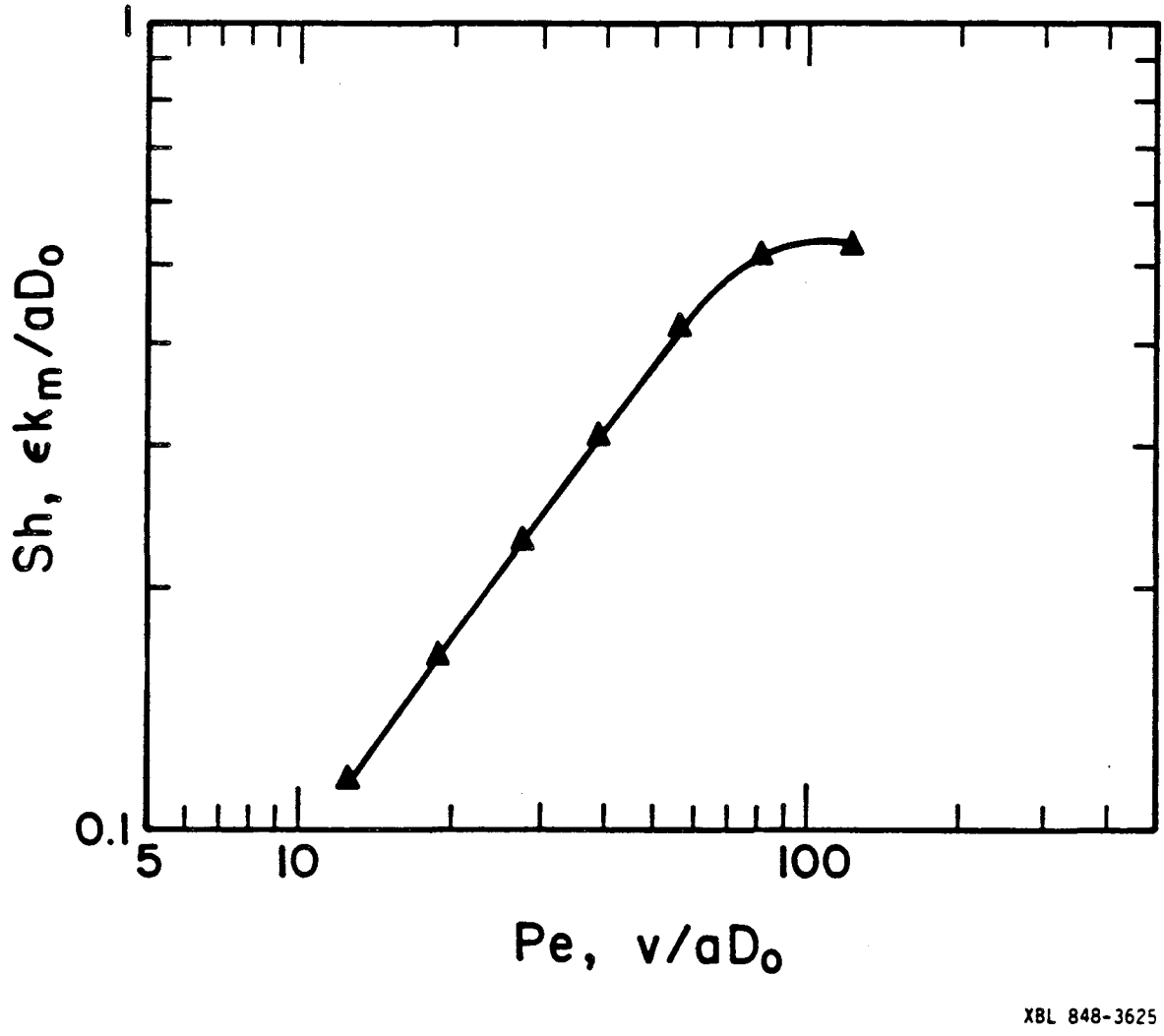

Figure 14. Effect of flowrate on the mass-transfer coefficient. Dimensionless Sherwood-number/Péclet-number plot. L = 12.7 cm, a = 66 cm^{-1}, ϵ = 0.97, D_o = 1.0×10^{-5} cm^2/s.

Comparison of Experiments to Model Predictions

One of the primary goals of this study is to check the applicability of the model of Trainham and Newman [14] to the study of flow-through porous electrodes made of RVC. To this end, figures 5, 6, 7, and 9 contain direct comparisons of experimental data to predictions from the model. In this section, an explanation is presented of the manner in which the fitting parameters for the model were chosen, and the quality of the fit is discussed. The comparison confirms the validity of the model and indicates that the exchange-current density for mercury deposition is much higher on solid glassy carbon than on RVC.

The presentation begins with an abbreviated description of the mathematical model, including the governing differential equations and definitions of the major parameters. The two major fitting parameters are the exchange-current densities for the main reaction ($i_{oR,ref}$) and for the side reaction ($i_{oS,ref}$), which are chosen by fitting the porous-electrode data in figure 5. Curves on the other figures are calculated from the model with these parameters. Ohmic-drop data (figure 7) provide an independent check on the validity of the model, and the close agreement between the calculations and experiment there support the applicability of the model.

Trainham and Newman's Model

The model employed for this study is very similar to the one-dimensional, macrohomogeneous model of a flow-through porous electrode for metal-ion removal developed by Trainham and Newman. Additional details and a complete derivation of the governing equations may be found in [14]. A source listing of the computer program used for the calculations is contained in [22].

The model, based on the earlier work by Newman and Tobias [23], considers the solution and electrode matrix as two superimposed continua, where the

details of the internal pore structure can be effectively averaged. The electrolyte is assumed to be well supported and the side reaction to be concentration-independent. As a result, the problem, in dimensionless form, can be stated as a set of two coupled, nonlinear ordinary differential equations: a material balance on the local concentration of metal-ion reactant,

$$\frac{d\theta}{dy} = -J_R , \tag{6}$$

and a charge balance determining the local overpotential,

$$\frac{d}{dy}\left(\frac{1}{P_2}\frac{d\eta'}{dy} + \theta\right) = J_S . \tag{7}$$

θ represents metal-ion concentration, η' potential driving force, and y distance through the packed bed. J_R, a reaction-rate term for the main reaction (metal deposition), is defined as

$$J_R = \frac{\theta - P_1 \exp\left[\left(\frac{\alpha_{aR}}{\alpha_{cR}} + 1\right)\eta'\right]}{1 + \exp(\eta')}, \tag{8}$$

and J_S, a reaction-rate term for the side reaction (hydrogen evolution), is defined as

$$J_S = P_3 \exp\left(-\frac{\alpha_{cS}}{\alpha_{cR}}\eta'\right)\left[1 - P_4 \exp\left(\frac{\alpha_{aS} + \alpha_{cS}}{\alpha_{cR}}\eta'\right)\right]. \tag{9}$$

The concentration at the inlet to the reactor is fixed, as expressed by the boundary condition:

$$\text{at } y = 0, \quad \theta = 1 . \tag{10}$$

Boundary conditions on the potential driving force depend on the placement of the counterelectrode and of the current collector. Two cases are considered here:

UD (upstream counterelectrode, downstream current collector), where,

at $y = 0$,

$$\frac{d\eta'}{dy} = P_5 I^* , \tag{11}$$

and, at $y = \alpha L$,

$$\frac{d\eta'}{dy} = -P_6 I^* , \tag{12}$$

and DU (downstream counterelectrode, upstream current collector), where,

at $y = 0$,

$$\frac{d\eta'}{dy} = P_6 I^* , \tag{13}$$

and, at $y = \alpha L$,

$$\frac{d\eta'}{dy} = -P_5 I^* . \tag{14}$$

P_1 characterizes the backward term of the main-reaction rate, P_2 the relative importance of ohmic resistance to mass-transfer resistance, P_3 the rate of the side reaction, and P_4 the backward term in the side-reaction rate. P_5 and P_6 represent the relative importance of the ohmic potential drop in the pore solution phase and the electrode matrix phase. The parameter α is the reciprocal of the penetration depth into the reactor, and I^* is the ratio of the actual current density to the current density that would exist if all of the metal-ion feed were completely reacted in the absence of a side reaction.

The model parameters and their definitions are summarized in tables 3 and 4. Although virtually identical to the definitions in [14], there is one important difference between the model equations and parameters shown here and those of Trainham and Newman. In this work, all of the effects of axial dispersion are included in the mass-transfer coefficient $\overline{k_m}$, whereas the original model employed local film coefficients k_m and considered the effect of dispersion

Table 3. Definitions of Special Quantities Derived for Model Calculations

Reciprocal of the Penetration Depth:

$$\alpha = \frac{a\overline{k}_m}{v}$$

Conductivity:

$$\kappa = \kappa_0 \epsilon^{1.5}$$

Open-Circuit Potentials:

$$U_R = U_R^0 - U_{re} + \frac{RT}{nF}\ln\left(\frac{c_{Rf}}{\rho_o}\right) - 2\frac{RT}{F}\ln\left(\frac{c_{a^-f}}{\rho_o}\right)$$

$$U_S = U_S^0 - U_{re} + \frac{RT}{F}\ln\left(\frac{c_{H^+f}}{\rho_o}\right) - \frac{RT}{2F}\ln\left(P_{H_2f}\right)$$

$$\Delta U = U_S - U_R$$

Exchange-Current Densities:

$$i_{oRf} = i_{oR,ref}\left(\frac{c_{Rf}}{c_{R,ref}}\right)^{\gamma_R}\left(\frac{c_{a^-f}}{c_{a^-ref}}\right)^{\gamma_{R,a^-}}$$

$$i_{oSf} = i_{oS,ref}\left(\frac{c_{H^+f}}{c_{H^+ref}}\right)^{\gamma_{S,H^+}}\left(\frac{P_{H_2f}}{P_{H_2,ref}}\right)^{\gamma_{S,H_2}}$$

where,

$$\gamma_R = -s_R + \frac{\alpha_{cR}s_R}{n} \qquad \gamma_{R,a^-} = 2\alpha_{cR}$$

$$\gamma_{S,H^+} = 1 - \alpha_{cS} \qquad \gamma_{S,H_2} = \frac{\alpha_{cS}}{2}$$

separately by introducing an additional parameter, D'. By incorporating the dispersion effects directly into the mass-transfer coefficient, the present model

allows the values of $\bar{k}_m$ from table 2 to be used without modification in the theoretical calculations. If, in [14], D' is taken to be zero and all instances of k_m are replaced by $\bar{k}_m$, the statement of the problem is identical to that shown here.

Model Parameters

Table 5 shows the parameter values chosen for the model presented in figures 5, 6, and 7. For the model results shown in all of the figures, physical property data and dimensional fitting parameters are the same. However, since operating conditions are not identical in all of the runs, values of some of the parameters for the model results shown in figure 9 differ from those shown in table 5. The changes are recorded in table 6.

Table 4. Definitions of Dimensionless Variables and Parameters

$$\theta = \frac{c_R}{c_{Rf}} \qquad \eta' = \frac{\alpha_{cR} F \eta}{RT} + \ln\left(-\frac{n F \bar{k}_m c_{Rf}}{s_R i_{oRf}}\right)$$

$$y = \frac{a \bar{k}_m x}{v} \qquad I^* = \frac{s_R i}{n F v c_{Rf}}$$

$$P_1 = \left(-\frac{s_R i_{oRf}}{n F \bar{k}_m c_{Rf}}\right)^{1 + \alpha_{aR}/\alpha_{cR}} \qquad P_2 = \frac{\alpha_{cR} n F^2 v^2 c_{Rf}}{s_R a \bar{k}_m RT}\left(\frac{1}{\kappa} + \frac{1}{\sigma}\right)$$

$$P_3 = -\frac{s_R i_{oSf}}{n F \bar{k}_m c_{Rf}} \exp\left(\frac{\alpha_{cS} F \Delta U}{RT}\right)\left(-\frac{n F \bar{k}_m c_{Rf}}{s_R i_{oRf}}\right)^{\alpha_{cS}/\alpha_{cR}}$$

$$P_4 = \left(-\frac{s_R i_{oRf}}{n F \bar{k}_m c_{Rf}}\right)^{\frac{\alpha_{aS} + \alpha_{cS}}{\alpha_{cR}}} \exp\left(-\frac{F(\alpha_{aS} + \alpha_{cS})\Delta U}{RT}\right)$$

$$P_5 = -\frac{\sigma P_2}{\sigma + \kappa} \qquad P_6 = -\frac{\kappa P_2}{\sigma + \kappa}$$

The mass-transfer coefficients are taken from the results of the concentration measurements in table 2 and, therefore, are consistent with the data shown in figures 10 and 14. The operating conditions and the physical property data are all known (see table 1), and, therefore, the only fitting parameters for the model are the kinetic constants for the main reaction ($i_{oR,ref}$, α_{aR}, α_{cR}), the kinetic constants for the side reaction ($i_{oS,ref}$, α_{aS}, α_{cS}), and the partial pressure of hydrogen ($P_{H_2 f}$) in the feed to the reactor.

Table 5. Values of Parameters for Model Calculations

s_R =	-1	n =	2
α =	0.5440 cm^{-1}	$1/\alpha$ =	1.838 cm
$i_{oR,ref}$ =	3×10^{-7} A/cm^2	$c_{R,ref}$ =	5×10^{-7} mol/cm^3
		c_{α^-ref} =	3.8×10^{-3} mol/cm^3
α_{aR} =	1.4	α_{cR} =	0.6
γ_R =	0.7	γ_{R,α^-} =	1.2
i_{oRf} =	2.00×10^{-7} A/cm^2	c_{Rf} =	2.273×10^{-7} mol/cm^3
		$c_{\alpha^- f}$ =	4.3×10^{-3} mol/cm^3
$i_{oS,ref}$ =	2×10^{-6} A/cm^2	$c_{H^+,ref}$ =	1×10^{-3} mol/cm^3 (pH = 0)
		$P_{H_2,ref}$ =	1 atm
α_{aS} =	0.5	α_{cS} =	0.5
γ_{S,H^+} =	0.5	γ_{S,H_2} =	0.25
i_{oSf} =	5.32×10^{-10} A/cm^2	$c_{H^+ f}$ =	1×10^{-7} mol/cm^3 (pH = 4)
		$P_{H_2 f}$ =	5×10^{-7} atm
U_R =	-0.00536 V	U_S =	-0.295 V
ΔU =	-0.290 V		
P_1 =	2.865×10^{-6}	P_2 =	-0.2803
P_3 =	4.984×10^{-6}	P_4 =	133.93
P_5 =	0.2526	P_6 =	0.02775
αL =	6.909		

Effect of Side Reaction

The transfer coefficients for the side reaction (α_{aS}, α_{cS}) are chosen to be 0.5, in keeping with generally accepted mechanisms for hydrogen reduction. The parameters P_{H_2f} and $i_{oS,ref}$ determine the length of the limiting-current plateau as described by White and Newman [24]. Since there is virtually no H_2 gas in the feed, the value of P_{H_2f} is very uncertain. It is important to note, however, that the side reaction occurs primarily in a Tafel range (backward term in the rate expression is small). Under these conditions, an increase in P_{H_2f} should have very little effect on the location of the side reaction. In fact, changing P_{H_2f} from 5×10^{-7} atm to 1×10^{-12} atm results in no shift in the location of the side reaction and a shift of only 4 mV in the open-circuit potential calculated from the model. As a result, the fitting parameter for the side reaction is primarily the exchange-current density $i_{oS,ref}$. It is chosen from a fit to figure 5, since no other experiments indicate a side reaction.

Table 6. Additional Parameter Values for Figure 9

c_{Rf} (mol/cm^3)	3.125×10^{-7}	3.125×10^{-7}	3.125×10^{-7}
i_{oRf} (A/cm^2)	2.50×10^{-7}	2.50×10^{-7}	2.50×10^{-7}
U_R (V)	-0.00127	-0.00127	-0.00127
ΔU (V)	-0.294	-0.294	-0.294
v (cm/s)	0.0214	0.0128	0.00576
k_m (cm/s)	1.805×10^{-4}	1.157×10^{-4}	5.747×10^{-5}
α (cm^{-1})	0.5567	0.5989	0.6587
$1/\alpha$ (cm)	1.796	1.670	1.518
P_1	3.463×10^{-6}	1.525×10^{-6}	1.571×10^{-6}
P_2	-0.3161	-0.1750	-0.0719
P_3	3.719×10^{-6}	4.005×10^{-6}	4.500×10^{-6}
P_4	1.726×10^{2}	3.623×10^{2}	1.163×10^{3}
P_5	0.2848	0.1577	0.0647
P_6	0.03130	0.01733	0.007116
αL	7.070	7.606	8.366

Little quantitative information about the side reaction can be determined from the small amount of data obtained in this study, but the experiments do show qualitatively that the side reaction is not a major consideration in the evaluation of the system for mercury removal. In this regard, the system studied here is a good candidate for checking the applicability of the model, since in the model the side reaction is considered only as a second-order effect. The relative unimportance of side reaction means that the behavior of the porous electrode depends primarily on the kinetic parameters for the main reaction, and the choices of values for these parameters are discussed below.

Kinetic Constants for the Main Reaction

Transfer coefficients for the main reaction (α_{aR}, α_{cR}) are obtained directly from a fit of the linear sweep voltammograms on the rotating disk.† The exchange-current density ($i_{oR,ref}$), however, is chosen from a fit of the left side of the polarization curve in figure 5. The model fit to one of the voltammograms (from figure 12) on the disk electrode is shown in figure 15, both for the exchange-current density that best fits the rotating-disk data and for the value chosen for the model of the porous electrode. The exchange-current density obtained from the rotating disk experiments is 5000 times higher than that required to fit figure 5. This difference indicates that, although both the porous bed and the disk electrode are made of a glassy carbon, the activity of the internal surface of the RVC foam and the activity of the polished disk surface are considerably different. Although this is not surprising, it does point out the importance of experimenting directly with the porous-bed material prior to scale-up.

† Methods for the numerical simulation of linear sweep voltammograms are described in more detail elsewhere.[22]

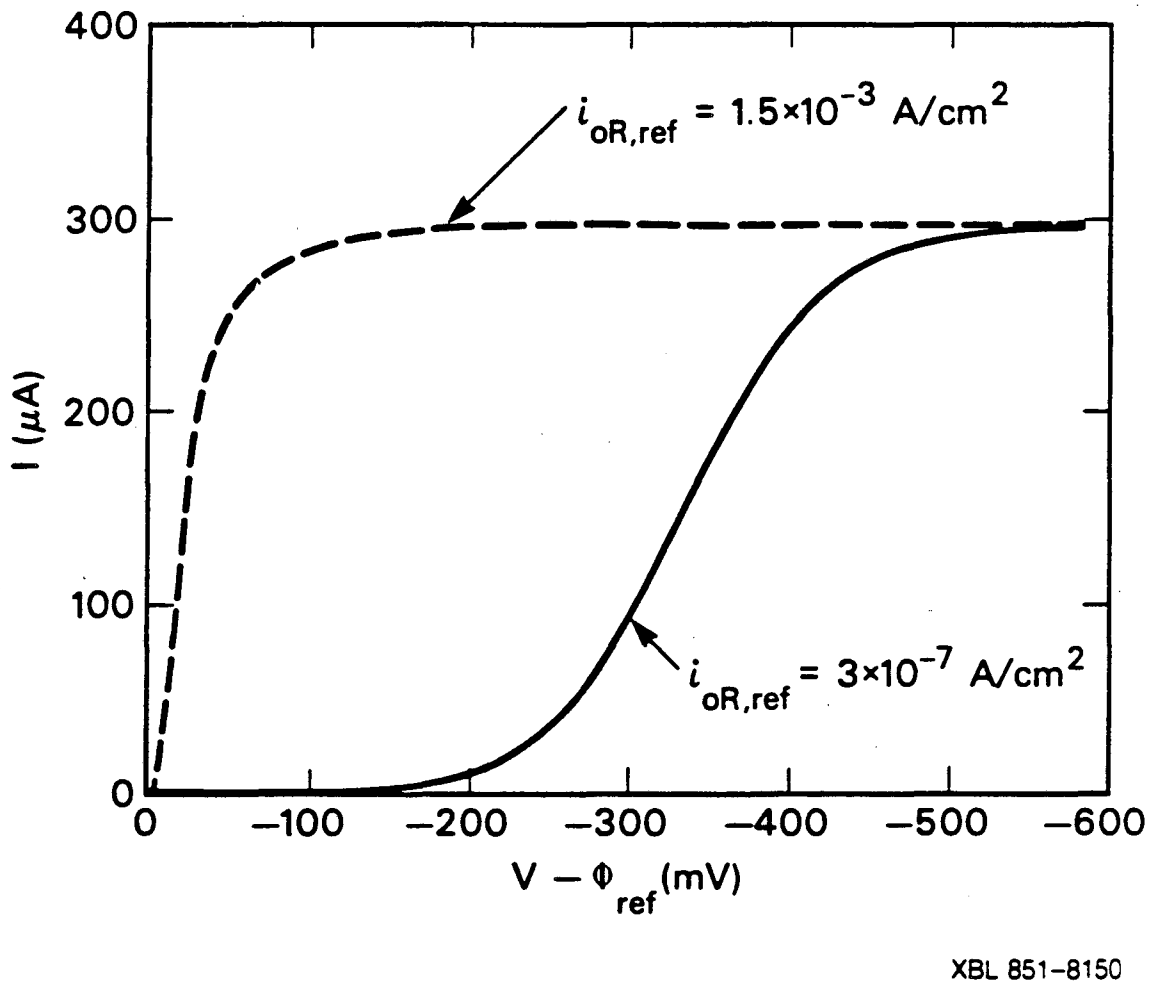

Figure 15. Effect of exchange-current density on model voltammograms. Dashed curve (best fit): $i_{oR,ref} = 1.5\times10^{-3}$ A/cm^2. Solid curve: $i_{oR,ref} = 3.0\times10^{-7}$ A/cm^2.

Consistency Check: Ohmic Potential Drop

If the conductivity of the electrode matrix is high relative to that of the solution (as in this study), resistance measurements can be used to determine kinetic parameters. In addition, the ohmic-drop measurements are independent of the polarization measurements, and, as a result, they provide a consistency check on the data obtained in this investigation. Thus, the close agreement between the model predictions and the experimental measurements of ohmic drop, as illustrated in figure 7, confirms the validity of the $i_{oR,ref}$ value chosen to fit figure 5.

The reason for the sensitivity of the ohmic potential drop to kinetic parameters is illustrated in figure 16a for the case of upstream counterelectrode placement. At low fractions of limiting current, the ohmic drop measurements are strongly influenced by kinetics, since the value of the resistance is very sensitive to the shape of the upstream concentration profile. This sensitivity arises from the influence of the kinetic rate on the effective penetration depth. Since, in the absence of side reaction, the resistance is proportional to penetration depth, changes in exchange-current density can give rise to substantial differences in ohmic drop.

The ohmic drop measurements are particularly useful if the electrode is very long. If the electrode is very long, the catholyte exit can attain equilibrium for any moderate value of $i_{oR,ref}$, and, therefore, the value of $(V - \Phi_{ref})$ at the catholyte exit is fixed (by thermodynamics), independent of $i_{oR,ref}$. In that case, although polarization curves such as figure 5 provide no information at all regarding $i_{oR,ref}$, the effect of $i_{oR,ref}$ on ohmic drop (figure 7) remains unchanged. Thus, it is possible that large differences in ohmic drop can be seen even when only slight differences in polarization behavior are observable.

At limiting current, the polarization (driving force) is sufficiently large that the concentration profile is completely determined by mass transfer, regardless

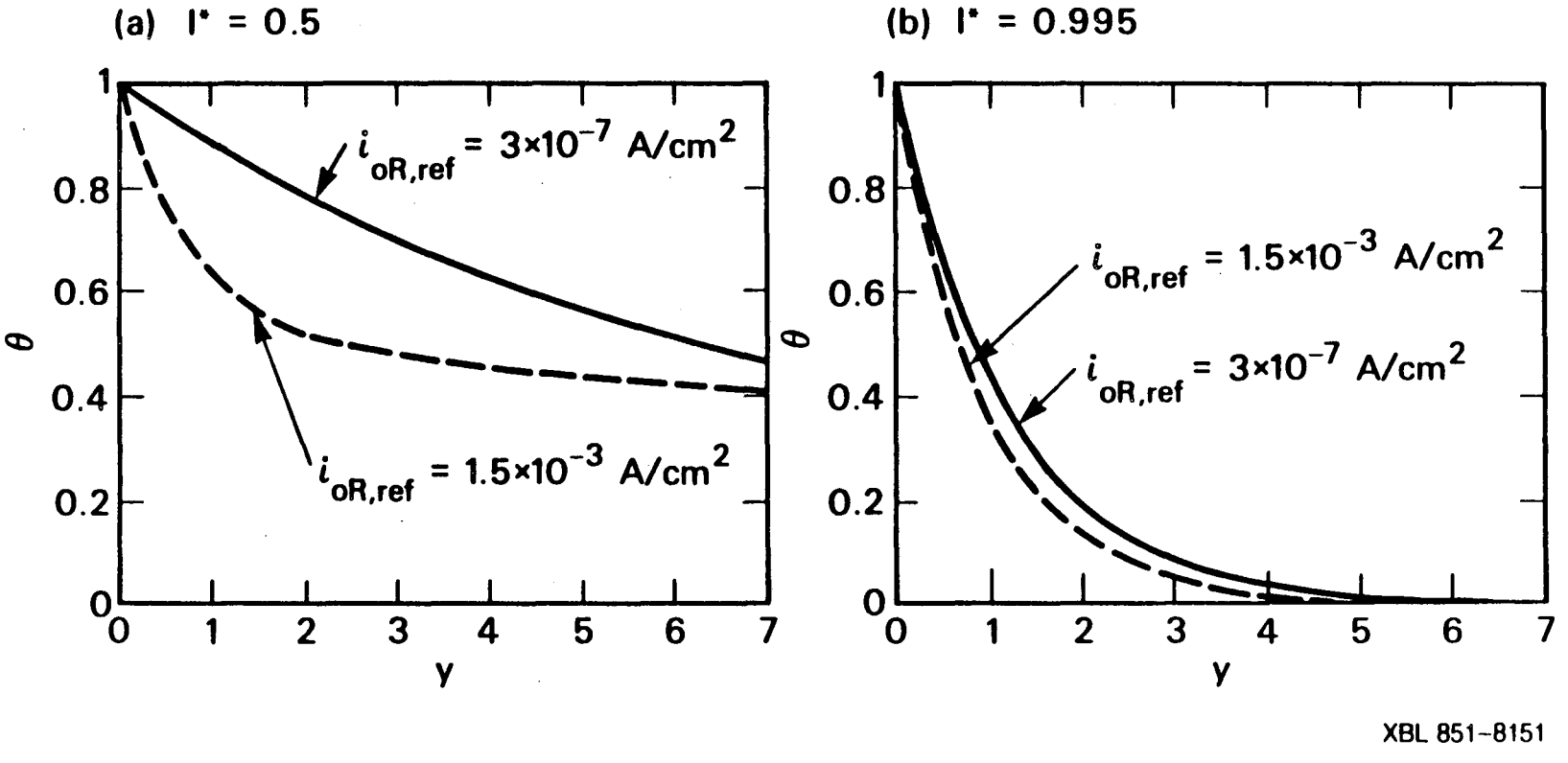

XBL 851-8151

Figure 16. Effect of kinetics on ohmic drop measurements.

of the kinetic parameters. Under these conditions, illustrated in figure 16b, ohmic drop measurements provide no information about kinetics, but they do provide a check on the values of the mass-transfer coefficients. By comparing the results for upstream and downstream counterelectrode placement, the ratio of the penetration depth to the bed length can be determined (see figure 8). Hence, the agreement between model and experiment in figure 7 at high overpotential (limiting-current conditions) supports the mass-transfer coefficient correlation in figure 14.

Conclusions

This study has demonstrated that a flow-through porous electrode made of reticulated vitreous carbon can be a very effective device for the removal of mercury contamination in brine solutions. The experiments indicate that the mercury system is also an excellent candidate for the general study of porous electrodes, since the chemistry is simple, side reactions are relatively unimportant, and a reliable method for concentration measurement is available. A bench-scale experimental electrode has been used to demonstrate the effectiveness of the device, to illustrate the effect of counterelectrode placement on the ohmic potential drop, to determine an empirical correlation (in graphical form) of the effect of electrolyte velocity on the mass-transfer coefficient in the electrode, and to verify the applicability of a one-dimensional mathematical model of the porous electrode. A comparison of the exchange-current density for mercury deposition on RVC to that on a solid glassy carbon indicates that the local rate of mercury deposition is slower on RVC.

Acknowledgments

The authors would like to thank Mr. Edward Brandenberger for suggesting the use of the gold-film analyzer for the mercury measurements. Special thanks are also due to Mr. Christopher Hofseth and to Mr. John Kelsey for their help with the rotating-disk experiments.

This work was supported by the United States Department of Energy under Contract Number DE-AC03-76SF00098 through the Director, Office of Energy Research, Office of Basic Energy Sciences, Chemical Sciences Division, and through the Assistant Secretary of Conservation and Renewable Energy, Office of Energy Systems Research, Energy Storage Division.

List of Symbols

a	Specific surface or interfacial area (per unit volume of the porous electrode), cm^2/cm^3
A	Area of rotating disk electrode, cm^2
$c_{Cl^-,f}$	Concentration of Cl^- ion in the catholyte feed to the porous electrode, mol/cm^3
$c_{Cl^-,ref}$	Reference concentration of Cl^-, mol/cm^3
c_b	Concentration of mercury in the bulk, far away from the rotating disk, mol/cm^3
$c_{H^+,f}$	Concentration of H^+ ion in the catholyte feed, mol/cm^3
$c_{H^+,ref}$	Reference concentration of H^+ ion, mol/cm^3
c_R	Concentration of main reactant, $HgCl_4^{-2}$, in the catholyte within the flow-through porous electrode, mol/cm^3
c_{Rf}	Concentration of main reactant, $HgCl_4^{-2}$, in catholyte entering the flow-through porous electrode, mol/cm^3
$c_{R,ref}$	Reference concentration of main reactant species, mol/cm^3
D_o	Diffusion coefficient of $HgCl_4^{-2}$ in the feed solution, cm^2/s
F	Faraday's constant, 96487 C/equiv
i	Superficial current density to the porous electrode, A/cm^2
i_{oRf}	Exchange-current density for the main reaction at the feed concentrations, A/cm^2
$i_{oR,ref}$	Exchange-current density for the main reaction at the reference concentrations, A/cm^2
i_{oSf}	Exchange-current density for the side reaction at the feed concentrations, A/cm^2
$i_{oS,ref}$	Exchange-current density for the side reaction at the reference concentrations, A/cm^2
I	Current, A

I_{lim}	Mass-transfer-limited current, A
I^*	Dimensionless applied current density (defined in table 4)
J_R	Dimensionless reaction-rate term for the main reaction
J_S	Dimensionless reaction-rate term for the side reaction
k_m	Local mass-transfer coefficient, cm/s
$\overline{k_m}$	Average mass-transfer coefficient, cm/s
L	Length of flow-through porous electrode, cm
n	Number of electrons transferred in the main electrode reaction
P_1	Parameter characterizing the backward term of the main reaction (defined in table 4)
P_2	Parameter characterizing the relative importance of ohmic resistance to mass-transfer resistance (defined in table 4)
P_3	Parameter characterizing the rate of side reaction (defined in table 4)
P_4	Parameter characterizing the backward term of the side reaction (defined in table 4)
P_5	Parameter representing the relative importance of ohmic drop in the solution phase (defined in table 4)
P_6	Parameter representing the relative importance of ohmic drop in the electrode matrix phase (defined in table 4)
Pe	Péclet Number, $Re \cdot Sc = v/aD_a$
P_{H_2f}	Partial pressure of hydrogen gas in the feed to the porous electrode, atm
$P_{H_2,ref}$	Reference partial pressure of hydrogen gas, atm
R	Universal gas constant, 8.314 J/mol-K
Re	Reynolds Number, $v/a\nu$
Q	Flowrate, cm^3/min

S	Cross-sectional area of porous electrode, cm^2
Sc	Schmidt Number, ν / D_o
Sh	Sherwood Number, $\epsilon \bar{k}_m / aD_o$
s_R	Stoichiometric coefficient of the main reactant species
T	Temperature, K
v	Superficial fluid velocity, cm/s
U_{re}	Potential of a calomel reference electrode (containing saturated KCl) (with respect to a standard hydrogen electrode), V
U_R	Equilibrium potential of the main reaction at the feed concentrations (relative to U_{re}), V
U_R^θ	Standard electrode potential for the main reaction, $HgCl_4^{-2}/Cl^-/Hg$, (with respect to a standard hydrogen electrode), V
U_S	Equilibrium potential of the side reaction at the feed concentrations (relative to U_{re}), V
U_S^θ	Standard electrode potential for the side reaction, H^+/H_2, 0.0 V
ΔU	Difference in equilibrium potential between the side reaction and the main reaction at the feed concentrations, V
V	Potential of working electrode, V
$V - \Phi_{ref}$	Potential between the working electrode and a saturated calomel reference electrode in the catholyte exit stream, V
x	Distance through electrode, cm
y	Dimensionless distance through porous electrode (defined in table 4)
α	Reciprocal of the penetration depth into the electrode (defined in table 3)
αL	Dimensionless electrode length
α_{aR}	Anodic transfer coefficient for the main reaction

α_{aS}	Anodic transfer coefficient for the side reaction
α_{cR}	Cathodic transfer coefficient for the main reaction
α_{cS}	Cathodic transfer coefficient for the side reaction
γ_R	Exponent in the composition dependence of species R ($HgCl_4^{-2}$) in the expression for $i_{oR,f}$ (defined in table 3)
γ_{R,Cl^-}	Exponent in the composition dependence of Cl^- in the expression for $i_{oR,f}$ (defined in table 3)
γ_{S,H^+}	Exponent in the composition dependence of H^+ in the expression for $i_{oS,f}$ (defined in table 3)
γ_{S,H_2}	Exponent in the composition dependence of H_2 in the expression for $i_{oS,f}$ (defined in table 3)
ϵ	Porosity or void-volume fraction
η'	Dimensionless potential driving force, (defined in table 4)
θ	Dimensionless concentration (defined in table 4)
κ	Effective conductivity of electrolyte within the porous electrode, mho/cm
κ_o	Conductivity of feed solution outside of the electrode, mho/cm
μ	Viscosity, g/cm-s
ν	Kinematic viscosity, μ/ρ_o, cm^2/s
ρ_o	Solvent density, kg/cm^3
σ	Effective conductivity of the solid matrix, mho/cm
Φ_{ref}	Reference potential, V
$\Phi'_{downstream}$	Potential in solution exiting electrode, V
$\Phi_{upstream}$	Potential in solution entering electrode, V
Ω	Angular velocity, rad/s

References

1. Douglas N. Bennion and John Newman, "Electrochemical removal of copper ions from very dilute solutions," *Journal of Applied Electrochemistry*, **2** (1972), 113-122.

2. Richard Alkire and Brian Gracon, "Flow-Through Porous Electrodes," *Journal of the Electrochemical Society*, **122** (1975), 1594-1601.

3. John Van Zee and John Newman, "Electrochemical Removal of Silver Ions from Photographic Fixing Solutions Using a Porous Flow-Through Electrode," *Journal of the Electrochemical Society*, **124** (1977), 706-708.

4. M. Enriquez-Granados, G. Valentin, and A. Storck, "Electrochemical Removal of Silver Using a Three-Dimensional Electrode," *Electrochimica Acta*, **28** (1983), 1407-1414.

5. James Trainham and John Newman, "The Removal of Lead Ions from Very Dilute Solutions Using a Porous Flow-Through Electrode," *Inorganic Materials Research Division Annual Report 1973*, 51-53. Lawrence Berkeley Laboratory, University of California, April, 1974, LBL-2299.

6. Gary George Trost, *Applications of Porous Electrodes to Metal-Ion Removal and the Design of Battery Systems*, dissertation, University of California, Berkeley (1983), LBL-16852.

7. J. Wang and H. D. Dewald, "Deposition of Metals at a Flow-Through Reticulated Vitreous Carbon Electrode Coupled with On-Line Monitoring of the Effluent," *Journal of the Electrochemical Society*, **130** (1983), 1814-1818.

8. A. T. Kuhn, "Antimony removal from dilute solutions using a restrained bed electrochemical reactor," *Journal of Applied Electrochemistry*, **4** (1974), 69-73.

9. James Arthur Trainham, *Flow-Through Porous Electrodes*, dissertation, University of California, Berkeley (1979), LBL-9565.

10. Michael Matlosz and John Newman, "Use of a Flow-Through Porous Electrode for Removal of Mercury from Contaminated Brine Solutions," *Proceedings of the Symposium on Transport Processes in Electrochemical Systems* (The Electrochemical Society, volume 82-10, 1982), 53-63.

11. John Newman and William Tiedemann, "Flow-through Porous Electrodes," *Advances in Electrochemistry and Electrochemical Engineering*, 11, Heinz Gerischer and Charles W. Tobias, editors (New York: John Wiley and Sons, Inc., 1978), 353-438.

12. Bertrand P. Scholder, "Etude d'une électrode à empilement de treillis pour la récupération des métaux en solutions diluées,", dissertation, Swiss Federal Institute of Technology (ETH), Zurich (1982).

13. Roman E. Sioda and Kenneth B. Keating, "Flow Electrolysis with Extended-surface Electrodes,", Allen J. Bard, ed., *Electroanalytical Chemistry, A Series of Advances* (New York: Marcel Dekker, Inc., 1982), **12**, 1-51.

14. James A. Trainham and John Newman, "A Flow-Through Porous Electrode Model: Application to Metal-Ion Removal from Dilute Streams," *Journal of the Electrochemical Society*, **124** (1977), 1528-1540.

15. James A. Trainham and John Newman, "The Effect of Electrode Placement and Finite Matrix Conductivity on the Performance of Flow-Through Porous

Electrodes," *Journal of the Electrochemical Society*, **125** (1978), 58-68.

16. P. J. Murphy, "Determination of Nanogram Quantities of Mercury in Liquid Matrices by a Gold Film Mercury Detector," *Analytical Chemistry*, **51** (1979), 1599-1600.

17. *Handbook of Chemistry and Physics*, 57 th edition, Robert C. Weast, editor (Cleveland, Ohio: CRC Press, Inc., 1976).

18. Joseph Wang, "Reticulated Vitreous Carbon -- A New Versatile Electrode Material," *Electrochimica Acta*, **26** (1981), 1721-1726.

19. Peter S. Fedkiw, *Mass Transfer Controlled Reactions in Packed Beds at Low Reynolds Numbers*, dissertation, University of California, Berkeley (1978), LBL-8509.

20. B. Levich, "The Theory of Concentration Polarization," *Acta Physicochimica U.R.S.S.*, **17** (1942), 257-307.

21. J. P. Sorensen and W. E. Stewart, "Computation of Forced Convection in Slow Flow Through Ducts and Packed Beds -- I Extensions of the Graetz Problem," *Chemical Engineering Science*, **29** (1974), 811-817.

22. Michael Matlosz, *Experimental Methods and Software Tools for the Analysis of Electrochemical Systems*, dissertation, University of California, Berkeley (1985), LBL-19375.

23. John S. Newman and Charles W. Tobias, "Theoretical Analysis of Current Distribution in Porous Electrodes," *Journal of the Electrochemical Society*, **109** (1962), 1183-1191.

24. Ralph White and John Newman, "Simultaneous Reactions on a Rotating-Disk Electrode," *Journal of Electroanalytical Chemistry*, **82** (1977), 173-186.

LAWRENCE BERKELEY LABORATORY
TECHNICAL INFORMATION DEPARTMENT
UNIVERSITY OF CALIFORNIA
BERKELEY, CALIFORNIA 94720